PHYSICAL REVIEW D **85,** 024046 (2012)

Modeling multipolar gravitational-wave emission from small mass-ratio mergers

Enrico Barausse,[1] Alessandra Buonanno,[1,2] Scott A. Hughes,[3] Gaurav Khanna,[4] Stephen O'Sullivan,[3] and Yi Pan[1]

[1]*Maryland Center for Fundamental Physics & Joint Space-Science Institute, Department of Physics, University of Maryland, College Park, Maryland 20742, USA*

[2]*Radcliffe Institute for Advanced Study, Harvard University, 8 Garden Street, Cambridge, Massachusetts 02138, USA*

[3]*Department of Physics and MIT Kavli Institute, 77 Massachusetts Avenue, Cambridge, Massachusetts 02139, USA*

[4]*Department of Physics, University of Massachusetts Dartmouth, North Dartmouth, Massachusetts 02747, USA*

(Received 13 October 2011; published 26 January 2012)

Using the effective-one-body (EOB) formalism and a time-domain Teukolsky code, we generate inspiral, merger, and ringdown waveforms in the small-mass-ratio limit. We use EOB inspiral and plunge trajectories to build the Teukolsky-equation source term, and compute full coalescence waveforms for a range of black-hole spins. By comparing EOB waveforms that were recently developed for comparable-mass binary black holes to these Teukolsky waveforms, we improve the EOB model for the (2, 2), (2, 1), (3, 3), and (4, 4) modes. Our results can be used to quickly and accurately extract useful information about merger waves for binaries with spin and should be useful for improving analytic models of such binaries.

DOI: 10.1103/PhysRevD.85.024046 PACS numbers: 04.25.Nx, 04.25.dg, 04.30.−w

I. INTRODUCTION

Since the numerical-relativity breakthrough of 2005 [1–3], there have been tremendous advances both in the computation of gravitational radiation from binary black-hole systems and in analytical modeling of this radiation using approximate techniques. Despite rapid and ongoing advances, it remains a challenge for numerical relativity to quickly and accurately compute models that span large regions of parameter space. Extreme conditions such as large spins and small-mass ratios are particularly challenging, although there has been excellent recent progress on these issues [4–6].

The effective-one-body (EOB) formalism [7–17] makes it possible to analytically model the three main phases of binary black-hole evolution: inspiral, plunge-merger, ringdown. EOB has been used to model the dynamics and gravitational-wave emission from comparable-mass binaries [18–28], extreme mass-ratio inspiraling binaries [29–31] (neglecting conservative self-force effects), and small-mass-ratio nonspinning binaries [32–36]. In order to study the transition from inspiral to plunge-merger and ringdown, Refs. [32,33] suggested combining EOB with black-hole perturbation theory. Concretely, they used EOB in order to compute the trajectory followed by an object spiraling and plunging into a much larger black hole, and then used that trajectory to describe the source for the time-domain Regge-Wheeler-Zerilli (RWZ) equation [37,38] describing metric perturbations to Schwarzschild black holes. They were then able to compute the full RWZ coalescence waveform and to compare with the EOB model. This was used in Ref. [34] to produce gravitational modes beyond the leading (2, 2) mode and compute the recoil velocity. More recently, Refs. [35,36] have used information from the RWZ modes to improve the modeling of the subleading EOB modes. A particularly beautiful feature of Ref. [36] is the use, for the first time, of hyperboloidal slicings in such an analysis. This effectively compactifies the computational domain so that waveforms at future null infinity can be read out of the numerical calculation with great accuracy.

References [39–41] developed a time-domain computational framework based on the Teukolsky equation [42], which describes curvature perturbations of rotating (Kerr) black holes. The goal of these papers has been to understand gravitational waves produced by physically reasonable but otherwise arbitrary trajectories of small bodies bound to rotating black holes (such as slowly inspiraling orbits or trajectories that plunge into the hole's event horizon). This has been used to understand the small-mass-ratio limit of merging black holes, studying, for example, the dependence of recoil velocity on black-hole spin in this limit. This Teukolsky code has been optimized to make effective use of modern many-core processor architectures, such as Graphics Processing Units (GPUs) [43].

In this paper, we combine EOB with the time-domain Teukolsky code developed in Refs. [39–41] to extend the ideas of Refs. [32,33,35,36] in several directions. Our primary extension is, for the first time, producing full coalescence waveforms describing inspiral, merger, and ringdown for quasicircular equatorial orbits in the Kerr spacetime. The energy flux we use in the EOB equations of motion comes from the factorized resummed waveforms of Refs. [13,15]. For the Schwarzschild limit, we model analytically three subleading modes [(2, 1), (3, 3), and (4, 4)] plus the dominant (2, 2) mode, finding useful information about the plunge-merger, which we use to improve the comparable-mass EOB model described in Ref. [28]. For more general spins, we calibrate the leading EOB mode for spins $a/M = -0.9$, -0.5, 0.5, and 0.7. We also extract some information regarding subleading modes and regarding the high prograde spin $a/M = 0.9$. These results for spinning binaries provide valuable input for improving the

spinning EOB model of Refs. [14,44], as well as the spinning EOB waveforms of Refs. [23,45]. This will in turn make it possible to develop models that can cover a much larger region of parameter space, including higher modes and extreme spins.

Several other groups have also been using perturbation-theory tools recently to improve our understanding for comparable-mass and intermediate-mass ratio binaries. For example, in Refs. [6,46,47] the authors directly employ a moving-puncture trajectory (or a post-Newtonian-inspired fit to it) in the RWZ equation. They compare the resulting RWZ waveform with the results of full numerical-relativity calculation for mass ratios $1/15$ and $1/10$, finding good agreement. Another recent suggestion is the hybrid approach of Ref. [48], in which inspiral-plunge intermediate-mass black-hole waveforms are computed by evolving the EOB equations of motion augmented by the perturbation-theory energy flux. An important issue in all attempts to model binary coalescence with perturbation theory is the computation of the so-called excitation coefficients, or more generally the question of which fundamental frequencies contribute to the radiation. In this context, perturbation-theory calculations are offering new insights [49–52].

The remainder of this paper is organized as follows. We begin in Sec. II by reviewing the EOB formalism for a test particle moving along quasicircular, equatorial orbits around a Kerr black hole. We then describe (Sec. III) the time-domain Teukolsky-equation calculation we use to compute the gravitational radiation emitted from a test particle that follows our EOB-generated trajectory. This section discusses in some detail numerical errors which arise from finite-difference discretization and from the extrapolation procedure by which we estimate our waves at future null infinity. Since we began this analysis, the Teukolsky code we use has been upgraded to use the hyperboloidal layer method [53]. This upgrade came too late to be used throughout our analysis but has been used to spot check our estimates of this extrapolation error.

Our results are presented in Sec. IV. We begin by comparing the leading and three subleading Teukolsky modes with $a/M = 0$ to the corresponding EOB modes calibrated to nonspinning comparable-mass binaries [28]. We then improve the nonspinning EOB model by including some features we find in our test-particle-limit calculation. We next calibrate the leading (2, 2) EOB waveform with our Teukolsky-equation results for spins $a/M = -0.9$, -0.5, 0.5, and 0.7. We conclude our results by discussing the challenges of calibrating subleading modes and of modeling extreme spin configurations, such as ones with $a/M \geq 0.9$. Section V summarizes our main conclusions and outlines some plans for future work. A particularly important goal for the future will be to move beyond equatorial configurations, modeling the important case of binaries with misaligned spins and orbits.

Throughout this paper, we use geometric units with $G = c = 1$.

II. DYNAMICS AND WAVEFORMS USING THE EFFECTIVE-ONE-BODY FORMALISM

The Hamiltonian of a nonspinning test-particle of mass μ orbiting a Kerr black hole of mass M and intrinsic angular momentum (or spin) per unit mass a is

$$H = \beta^i p_i + \alpha\sqrt{\mu^2 + \gamma^{ij} p_i p_j}, \tag{1}$$

where the indices i, j label spatial directions, and the functions introduced here are given by

$$\alpha = \frac{1}{\sqrt{-g^{tt}}}, \tag{2a}$$

$$\beta^i = \frac{g^{ti}}{g^{tt}}, \tag{2b}$$

$$\gamma^{ij} = g^{ij} - \frac{g^{ti} g^{tj}}{g^{tt}}; \tag{2c}$$

t is the time index, and $g_{\mu\nu}$ is the Kerr metric. Working in Boyer-Lindquist coordinates (t, r, θ, ϕ) and restricting ourselves to the equatorial plane $\theta = \pi/2$, the relevant metric components read

$$g^{tt} = -\frac{\Lambda}{r^2\Delta}, \tag{3a}$$

$$g^{rr} = \frac{\Delta}{r^2}, \tag{3b}$$

$$g^{\phi\phi} = \frac{1}{\Lambda}\left(-\frac{4a^2M^2}{\Delta} + r^2\right), \tag{3c}$$

$$g^{t\phi} = -\frac{2aM}{r\Delta}, \tag{3d}$$

where we have introduced the metric potentials

$$\Delta = r^2 - 2Mr - a^2, \tag{4}$$

$$\Lambda = (r^2 + a^2)^2 - a^2\Delta. \tag{5}$$

We replace the radial momentum p_r with p_{r^*}, the momentum conjugate to the *tortoise* radial coordinate r^*. The tortoise coordinate is related to the Boyer-Lindquist r by

$$dr^* = \frac{r^2 + a^2}{\Delta} dr. \tag{6}$$

Since p_r diverges at the horizon while p_{r^*} does not, this replacement improves the numerical stability of the Hamilton equations

$$\frac{dr}{dt} = \frac{\Delta}{r^2 + a^2}\frac{\partial H}{\partial p_{r^*}}(r, p_{r^*}, p_\phi), \tag{7a}$$

$$\frac{d\phi}{dt} = M\Omega = \frac{\partial H}{\partial p_\phi}(r, p_{r^*}, p_\phi), \tag{7b}$$

$$\frac{dp_{r^*}}{dt} = -\frac{\Delta}{r^2 + a^2}\frac{\partial H}{\partial r}(r, p_{r^*}, p_\phi) + {}^{\rm nK}\mathcal{F}_\phi \frac{p_{r^*}}{p_\phi}, \tag{7c}$$

$$\frac{dp_\phi}{dt} = {}^{\rm nK}\mathcal{F}_\phi. \tag{7d}$$

Our trajectory is produced by integrating these equations using initial conditions that specify a circular orbit. We typically find in our evolutions a small residual eccentricity on the order of 3×10^{-4}.

In Eqs. (7a)–(7d), radiation-reaction effects are included following the EOB formalism. For the ϕ component of the radiation-reaction force we use the non-Keplerian (nK) force

$${}^{\rm nK}\mathcal{F}_\phi = -\frac{1}{\nu v_\Omega^3}\frac{dE}{dt}, \tag{8}$$

where $v_\Omega \equiv (M\Omega)^{1/3}$, and dE/dt is the energy flux for quasicircular orbits obtained by summing over gravitational-wave modes (l, m). We use

$$\frac{dE}{dt} = \frac{1}{16\pi}\sum_{\ell=2}^{8}\sum_{m=-\ell}^{\ell} m^2 v_\Omega^6 |h_{\ell m}|^2. \tag{9}$$

The non-Keplerian behavior of the radiation-reaction force is implicitly introduced through the definition of $h_{\ell m}$. To describe the inspiral and plunge dynamics, we use the modes

$$h_{\ell m}^{\rm insp\text{-}plunge} = h_{\ell m}^{\rm F} N_{\ell m}. \tag{10}$$

The coefficients $N_{\ell m}$ describe effects that go beyond the quasicircular assumption and will be defined below [see Eq. (17)]. The factors $h_{\ell m}^{\rm F}$ are the factorized resummed modes and are given by [13]

$$h_{\ell m}^{\rm F} = h_{\ell m}^{(N,\epsilon)} \hat{S}^{(\epsilon)} T_{\ell m} e^{i\delta_{\ell m}} (\rho_{\ell m})^\ell. \tag{11}$$

Here, $\epsilon = \pi(\ell + m)$ is the parity of the multipolar waveform. The leading term in Eq. (11), $h_{\ell m}^{(N,\epsilon)}$, is the Newtonian contribution

$$h_{\ell m}^{(N,\epsilon)} = \frac{M\nu}{\mathcal{R}} n_{\ell m}^{(\epsilon)} c_{\ell+\epsilon}(\nu) V_\phi^\ell Y^{\ell-\epsilon,-m}\left(\frac{\pi}{2}, \phi\right), \tag{12}$$

where $\mathcal{R}$ is distance from the source, $Y^{\ell m}(\theta, \phi)$ are the scalar spherical harmonics, and the functions $n_{\ell m}^{(\epsilon)}$ and $c_{\ell+\epsilon}(\nu)$ are given in Eqs. (4a), (4b) and (5) of Ref. [54] with $\nu = \mu/M$. For reasons that we will explain in Sec. IV A, we choose

$$V_\phi^\ell = v_\phi^{(\ell+\epsilon)} \qquad (\ell, m) \neq (2, 1), (4, 4), \tag{13a}$$

$$V_\phi^\ell = \frac{1}{r_\Omega} v_\phi^{(\ell+\epsilon-2)} \qquad (\ell, m) = (2, 1), (4, 4). \tag{13b}$$

The quantities v_ϕ and r_Ω introduced here are defined by

$$v_\phi \equiv M\Omega r_\Omega \equiv M\Omega[(r/M)^{3/2} + a/M]^{2/3}. \tag{14}$$

The function $\hat{S}^{(\epsilon)}$ in Eq. (11) is given by

$$\hat{S}^{(\epsilon)}(r, p_{r^*}, p_\phi) = \begin{cases} H(r, p_{r^*}, p_\phi), & \epsilon = 0, \\ L = p_\phi v_\Omega, & \epsilon = 1. \end{cases} \tag{15}$$

The factor $T_{\ell m}$ in Eq. (11) resums the leading order logarithms of tail effects and is given by

$$T_{\ell m} = \frac{\Gamma(\ell + 1 - 2imM\Omega)}{\Gamma(\ell + 1)} \times e^{\pi m M\Omega} e^{2imM\Omega \log(2m\Omega r_0)}, \tag{16}$$

where $r_0 = 2M/\sqrt{e}$ [54] and $\Gamma(z) \equiv \int_0^\infty t^{z-1} e^{-t} dt$ is the complex gamma function. The factor $e^{i\delta_{\ell m}}$ in Eq. (11) is a phase correction due to subleading order logarithms; $\delta_{\ell m}$ is computed using Eqs. (27a)–(27i) of Ref. [54]. The factor $(\rho_{\ell m})^\ell$ in Eq. (11) collects the remaining post-Newtonian terms, and is computed using Eqs. (29a)-(29i) and Eqs. (D1a)-(D1m) of Ref. [54].

Finally, the function $N_{\ell m}$ entering Eq. (10) is given by

$$\begin{aligned} N_{\ell m} = \Bigg[& 1 + a_1^{h_{\ell m}} \frac{p_{r^*}^2}{(r\Omega)^2} + a_2^{h_{\ell m}} \frac{p_{r^*}^2}{(r\Omega)^2}\frac{M}{r} + a_3^{h_{\ell m}} \frac{p_{r^*}^2}{(r\Omega)^2}\left(\frac{M}{r}\right)^{3/2} \\ & + a_4^{h_{\ell m}} \frac{p_{r^*}^2}{(r\Omega)^2}\left(\frac{M}{r}\right)^2 + a_5^{h_{\ell m}} \frac{p_{r^*}^2}{(r\Omega)^2}\left(\frac{M}{r}\right)^{5/2}\Bigg] \\ & \times \exp\Bigg[i\Bigg(b_1^{h_{\ell m}} \frac{p_{r^*}}{r\Omega} + b_2^{h_{\ell m}} \frac{p_{r^*}^3}{r\Omega} + b_3^{h_{\ell m}} \sqrt{\frac{M}{r}} \frac{p_{r^*}^3}{r\Omega} \\ & + b_4^{h_{\ell m}} \frac{M}{r}\frac{p_{r^*}^3}{r\Omega}\Bigg)\Bigg], \end{aligned} \tag{17}$$

where the quantities $a_i^{h_{\ell m}}$ and $b_i^{h_{\ell m}}$ are nonquasicircular (NQC) orbit coefficients. We will explain in detail how these coefficients are fixed in Sec. IV.

We conclude this section by describing how we build the final merger-ringdown portion of the EOB waveform. For each mode (ℓ, m) we have

$$h_{\ell m}^{\rm merger\text{-}RD}(t) = \sum_{n=0}^{N-1} A_{\ell mn} e^{-i\sigma_{\ell mn}(t - t_{\rm match}^{\ell m})}, \tag{18}$$

where n labels the overtone of the Kerr quasinormal mode (QNM), N is the number of overtones included in our model, and $A_{\ell mn}$ are complex amplitudes to be determined by a matching procedure described below. The complex frequencies $\sigma_{\ell mn} = \omega_{\ell mn} - i/\tau_{\ell mn}$, where the quantities $\omega_{\ell mn} > 0$ are the oscillation frequencies and $\tau_{\ell mn} > 0$ are the decay times, are known functions of the final black-hole mass and spin and can be found in Ref. [55]. In this

paper, we model the ringdown modes as a linear combination of eight QNMs (i.e., $N = 8$).

The complex amplitudes $A_{\ell mn}$ in Eq. (18) are determined by matching the merger-ringdown waveform (18) with the inspiral-plunge waveform (10). In order to do this, N independent complex equations needs to be specified throughout the comb of width $\Delta t^{\ell m}_{\rm match}$. Details on the procedure are given in Ref. [28]. The full inspiral(-plunge)-merger-ringdown waveform is then given by

$$h_{\ell m} = h^{\text{insp-plunge}}_{\ell m}\theta(t^{\ell m}_{\rm match} - t) + h^{\text{merger-RD}}_{\ell m}\theta(t - t^{\ell m}_{\rm match}). \quad (19)$$

In this analysis, we focus on waveforms emitted by a test-particle of mass μ orbiting a Kerr black hole. Thus, we shall set to zero terms proportional to $\nu = \mu/M$ in Eq. (11), excepting the leading ν term in Eq. (12). Throughout this paper we restrict ourselves to the case $\nu = 10^{-3}$.

III. THE TIME-DOMAIN TEUKOLSKY CODE

A. Overview: The Teukolsky equation and its solution

The evolution of scalar, vector, and tensor perturbations of a Kerr black hole is described by the Teukolsky master equation [42], which takes the following form in Boyer-Lindquist coordinates:

$$\begin{aligned}
&-\left[\frac{(r^2+a^2)^2}{\Delta} - a^2\sin^2\theta\right]\partial_{tt}\Psi - \frac{4Mar}{\Delta}\partial_{t\phi}\Psi \\
&- 2s\left[r - \frac{M(r^2-a^2)}{\Delta} + ia\cos\theta\right]\partial_t\Psi + \Delta^{-s}\partial_r(\Delta^{s+1}\partial_r\Psi) \\
&+ \frac{1}{\sin\theta}\partial_\theta(\sin\theta\partial_\theta\Psi) + \left[\frac{1}{\sin^2\theta} - \frac{a^2}{\Delta}\right]\partial_{\phi\phi}\Psi \\
&+ 2s\left[\frac{a(r-M)}{\Delta} + \frac{i\cos\theta}{\sin^2\theta}\right]\partial_\phi\Psi - (s^2\cot^2\theta - s)\Psi \\
&= -4\pi(r^2 + a^2\cos^2\theta)T. \qquad (20)
\end{aligned}$$

The coordinates, the mass M, the spin parameter a, and the function Δ are as defined in the previous section. The number s is the "spin weight" of the field. When $s = \pm 2$, this equation describes radiative degrees of freedom for gravity. We focus on the case $s = -2$, for which $\Psi = (r - ia\cos\theta)^4\psi_4$, where ψ_4 is the Weyl curvature scalar that characterizes outgoing gravitational waves.

To solve Eq. (20), we use an approach introduced by Krivan *et al.* [56]. First, we change from radial coordinate r to tortoise coordinate r^* [Eq. (6)] and from axial coordinate ϕ to $\tilde{\phi}$, defined by

$$d\tilde{\phi} = d\phi + \frac{a}{\Delta}dr. \qquad (21)$$

These coordinates are much better suited to numerical evolutions, as detailed in Ref. [56]. Next, we exploit axisymmetry to expand Ψ in azimuthal modes:

$$\Psi(t, r, \theta, \tilde{\phi}) = \sum_m e^{im\tilde{\phi}} r^3 \phi_m(t, r, \theta). \qquad (22)$$

This reduces Eq. (20) to a set of decoupled $(2 + 1)$ dimensional hyperbolic partial differential equations (PDEs). We rewrite this system in first-order form by introducing a momentum-like field,

$$\Pi_m \equiv \partial_t\phi_m + \frac{(r^2+a^2)}{\Sigma}\partial_{r^*}\phi_m, \qquad (23)$$

where $\Sigma^2 = (r^2 + a^2)^2 - a^2\Delta\sin^2\theta$. We then integrate this system using a two-step, 2nd-order Lax-Wendroff finite-difference method. Details are presented in Refs. [39,40]. Following Ref. [56], we set ϕ_m and Π_m to zero on the inner and outer radial boundaries. Symmetries of the spheroidal harmonics are used to determine the angular boundary conditions: For m even, we have $\partial_\theta\phi_m = 0$ at $\theta = 0, \pi$; for m odd, $\phi_m = 0$ at $\theta = 0, \pi$.

The right-hand side (RHS) of Eq. (20) is a source term constructed from the energy-momentum tensor describing a pointlike object moving in the Kerr spacetime. The expression for T is lengthy and not particularly illuminating. For this paper, it is suffices to point out that T is constructed from Dirac-delta functions in r and θ, as well as first and second derivatives of the delta function in these variables. These terms have coefficients that are complex functions of the black hole's parameters and the location of the pointlike object. Details and discussion of how we model the deltas and their derivatives on a numerical grid are given in Ref. [39]. The delta functions are sourced at the location of the pointlike object; the source T thus depends on the trajectory that this body follows in the Kerr spacetime. In this analysis, we use a trajectory constructed using the EOB formalism to specify the small body's location.

One point worth emphasizing is that the source term is scaled by a factor of $1/\dot{t}$ [see Eq. (2.39) of Ref. [39]]; i.e., the source is inversely weighted by the rate of change of coordinate time per unit proper time experienced by the orbiting object. This means that the source term "redshifts away" as the object approaches the horizon. As a consequence, when describing a body that falls into a black hole, the Teukolsky equation (20) smoothly transitions into its homogeneous form, connecting the gravitational radiation from the last few orbital cycles to the Kerr hole's quasinormal modes in a very natural way. The same behavior is seen in other analyses which model plunging trajectories using black-hole perturbation theory (e.g., Refs. [34,49,57]).

We implement this numerical scheme with a FORTRAN code, parallelized using a standard domain decomposition (on the radial coordinate grid), and with OPENMPI[1] enabled message passing. Good scaling has been observed for several hundred processor cores. In this analysis, we used 128 processor cores for computing each m mode for all cases we studied.

[1]The open source version of MPI, the Message Passing Interface: http://openmpi.org.

B. Waveforms and multipole decomposition

Far from the black hole, ψ_4 is directly related to h_+ and $h_\times$ via

$$\psi_4 = \frac{1}{2}\left(\frac{\partial^2 h_+}{\partial t^2} - i\frac{\partial^2 h_\times}{\partial t^2}\right) \equiv \frac{1}{2}\frac{\partial^2 h}{\partial t^2}. \tag{24}$$

The waveform $h \equiv h_+ - ih_\times$ is then found by integrating ψ_4 twice, choosing constants of integration so that $h \to 0$ at very late times (long after the system's waves have decayed to zero).

As detailed in Sec. III A, our computation naturally decomposes the field Ψ (and hence ψ_4 and the waveform h) into axial modes with index m. For comparison with EOB waveforms, it is necessary to further decompose into modes of spin-weighted spherical harmonics. Following standard practice, we define

$$\psi_4 = \frac{1}{\mathcal{R}}\sum_{\ell,m} C_{\ell m}(t, r)\,{}_{-2}Y_{\ell m}(\theta, \phi), \tag{25}$$

$$h = \frac{1}{\mathcal{R}}\sum_{\ell,m} h_{\ell m}(t, r)\,{}_{-2}Y_{\ell m}(\theta, \phi). \tag{26}$$

In these equations, ${}_{-2}Y_{\ell m}$ is a spherical harmonic of spin-weight -2. Defining the inner product

$$\langle Y_{\ell m}|f\rangle = \int d\Omega\, {}_{-2}Y^*_{\ell m}(\theta, \phi) f \tag{27}$$

(where $*$ denotes complex conjugation), extracting $C_{\ell m}$ and $h_{\ell m}$ is simple:

$$C_{\ell m}(t, r) = \mathcal{R}\langle Y_{\ell m}|\psi_4\rangle, \tag{28}$$

$$h_{\ell m}(t, r) = \mathcal{R}\langle Y_{\ell m}|h\rangle. \tag{29}$$

The complex wave mode $h_{\ell m}$ can also be obtained from $C_{\ell m}$ by integrating twice, again choosing the constants of integration so that $h_{\ell m} \to 0$ at very late times.

C. Numerical errors

Our numerical solutions are contaminated by two dominant sources of error: Discretization error due to our finite-difference grid, and extraction error due to computing Ψ and associated quantities at finite spatial location rather than at null infinity.

1. Discretization error

As discussed in Ref. [40], our time-domain Teukolsky solver is intrinsically second-order accurate. Since we compute our solutions on a two-dimensional grid in tortoise radius r^* and angle θ, we expect our raw numerical output to have errors of order $(dr^*)^2$, $(d\theta)^2$, and $(dr^* d\theta)$. We mitigate this error with a variant of Richardson extrapolation, which we now describe.

Consider waveforms generated at three resolutions: $h^{(2)}_1$ at $(dr^*, d\theta) = (0.064M, 0.2)$; $h^{(2)}_2$ at $(0.032M, 0.1)$; and $h^{(2)}_3$ at $(0.016M, 0.05)$. Superscript "(i)" means the solution is ith-order accurate. We convert from second-order to third-order accuracy using [58]

$$h^{(3)}_{1.5} = h^{(2)}_1 - \frac{h^{(2)}_1 - h^{(2)}_2}{1 - 1/n^2}, \quad h^{(3)}_{2.5} = h^{(2)}_2 - \frac{h^{(2)}_2 - h^{(2)}_3}{1 - 1/n^2}. \tag{30}$$

Here, $n = 2$ is the ratio of grid spacing between the two resolutions.

To estimate the remaining error in this extrapolated solution, we compare $h^{(3)}_{2.5}$ and $h^{(3)}_{1.5}$. Let us define

$$\Delta h = h^{(3)}_{2.5} - h^{(3)}_{1.5}, \tag{31}$$

$$h^{(4)} = h^{(3)}_{2.5} - \frac{h^{(3)}_{2.5} - h^{(3)}_2}{1 - 1/n^3}. \tag{32}$$

$h^{(4)}$ is a fourth-order estimate of the Teukolsky solution h, assuming that errors in $h^{(3)}_{2.5,1.5}$ are third order. Defining the amplitude $|h|$ and phase ϕ as

$$h = |h|e^{i\phi}, \tag{33}$$

the amplitude error $\delta|h|/|h|$ and phase error $\delta\phi$ are

$$\frac{\delta|h|}{|h|} = \mathrm{Re}\left(\frac{\Delta h}{h^{(4)}}\right), \tag{34}$$

$$\delta\phi = \mathrm{Im}\left(\frac{\Delta h}{h^{(4)}}\right). \tag{35}$$

Figure 1 shows discretization errors for several gravitational modes $h_{\ell m}$ extracted at $r^* = 950M$. For this case, the large black hole is nonspinning ($a = 0$). Amplitude discretization errors are steady over almost the entire waveform, until very late times. In all cases, $\delta|h|/|h| \lesssim$ a few $\times 10^{-3}$. Similar behavior is observed for phase errors. For most modes, $\delta\phi \lesssim$ a few $\times 10^{-3}$ radians over the coalescence. The highest (ℓ, m) modes we consider approach 10^{-2} radian error at the latest times. Because higher (ℓ, m) modes require higher grid densities to be resolved, they tend to have larger discretization errors.

2. Extraction error

The code used in the bulk of this analysis extracts Ψ (and derived quantities such as ψ_4 and h) at large but finite radius. These quantities are more properly extracted at future null infinity. Although it has very recently become possible to extract waveforms at future null infinity (see Refs. [36,53]), we did not have this capability when we began this analysis. Instead, following Ref. [59], we extract waveforms at multiple radii, and fit to a polynomial in $1/r$. Again defining amplitude $|h|$ and phase ϕ using Eq. (33), we put

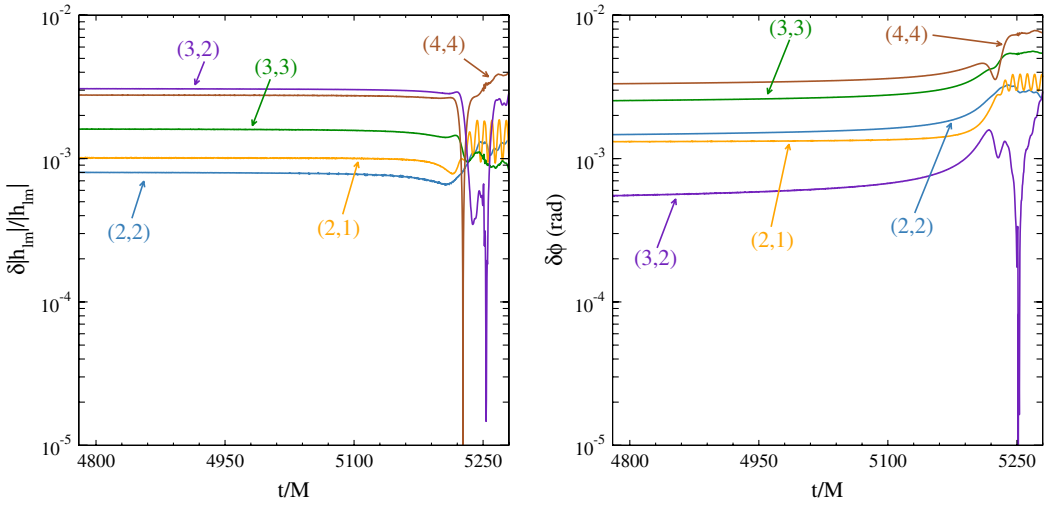

FIG. 1 (color online). Errors in amplitude (left panel) and phase (right panel) due to grid discretization for $a = 0$ at mass ratio $\mu/M = 10^{-3}$. These errors are the residual we find following the Richardson extrapolation procedure described in the text.

$$|h|(t - r^*, r) = |h|_{(0)}(t - r^*) + \sum_{k=1}^{N} \frac{|h|_{(k)}(t - r^*)}{r^k}, \quad (36)$$

$$\phi(t - r^*, r) = \phi_{(0)}(t - r^*) + \sum_{k=1}^{N} \frac{\phi_{(k)}(t - r^*)}{r^k}. \quad (37)$$

The time $t - r^*$ is retarded time, taking into account the finite speed of propagation to tortoise radius r^*, N is the order of the polynomial fit we choose. The functions $|h|_{(0)}(t - r^*)$ and $\phi_{(0)}(t - r^*)$ are the asymptotic amplitudes and phases describing the waves at future null infinity.

We extract waveforms at radii $r = 150M$, $350M$, $550M$, $750M$, and $950M$. We then perform nonlinear, least-squares fits for $|h|_{(k)}$ and $\phi_{(k)}$ using the Levenberg-Marquardt method [60] to find the asymptotic waveform amplitudes and phases. Following Ref. [59], we use $N = 3$ for the order of our fit and estimate errors by comparing the fits for $N = 3$ and $N = 2$.

Figure 2 shows the extrapolation errors we find for the same case shown in Fig. 1. For most of the evolution, extrapolation errors are smaller than discretization errors. In particular, the amplitude errors are at or below 10^{-3} for most of the coalescence; phase errors are at or below 10^{-3} radians. Both phase and amplitude errors grow to roughly 10^{-2} very late in the evolution. Note that the largest errors in ψ_4 come at the latest times, when the waves have largely decayed away. In other words, the largest errors occur when the waves are weakest. Because we compute ψ_4 and then infer amplitude and phase, both amplitude and phase are affected in roughly equal measure by these late time errors [see Eqs. (34) and (35)]. Our numerical errors appear to be of similar size to error estimates seen in related analyses (e.g., Ref. [36]).

Finally, it is worth noting that, thanks to the hyperboloidal layer method introduced to time-domain black-hole perturbation theory in Refs. [36,53], it will not be necessary to perform this extrapolation in future work. The codes will, to very good accuracy, compute the waveform directly at future null infinity. Although this advance did not come in time for the bulk of our present analysis, we have used it to check our error estimates in several cases. We find that our total numerical error estimates (discretization plus extrapolation error, combined in quadrature) is similar to the errors we compute using the hyperboloidal layer method.[2] This gives us confidence that our error estimates are reliable.

D. Comparing time-domain and frequency-domain Teukolsky codes

As a further check on the accuracy of our numerical Teukolsky-based waveforms, we compare time-domain (TD) waveforms computed using the techniques described here with frequency-domain (FD) waveforms [61,62]. Since we only calibrate the higher-order modes in the EOB model for $a = 0$, we focus on that case here. We expect our conclusions to be similar for spinning cases since we use the same procedure to estimate errors in that case.

As described in Secs. I and III A, in our analysis the source term for the TD waveforms [cf. Eq. (20)] depends on the EOB inspiral and plunge trajectory. For FD

[2]It is worth emphasizing that codes which use the hyperboloidal layer method are much faster than those which use the extrapolation described here; we find a speed-up of roughly ten (for the scale of the evolutions performed in the context of this work). Although it is gratifying that these extrapolations reliably improve our numerical accuracy, the substantial speed-up means that upgrading our method is worthwhile for future work.

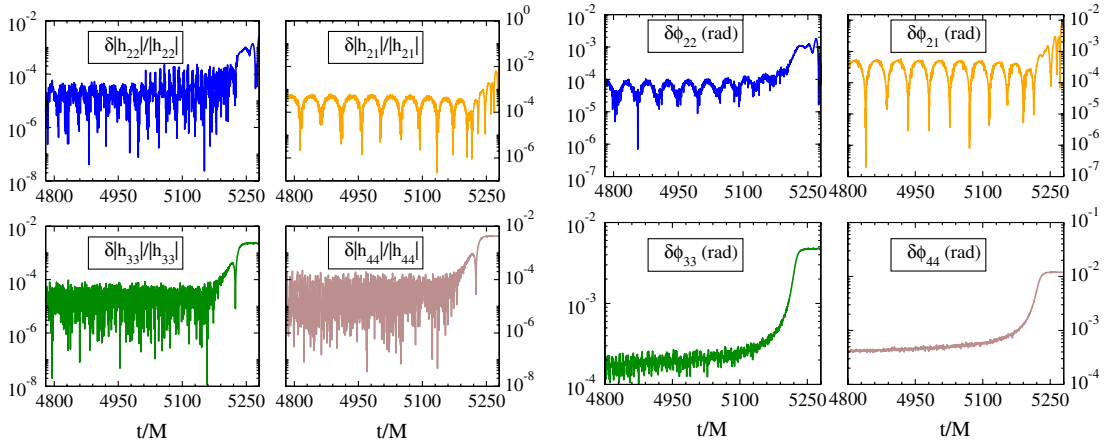

FIG. 2 (color online). Errors in amplitude (left panel) and phase (right panel) following extrapolation to infinity for the nonspinning case at mass ratio $\mu/M = 10^{-3}$.

waveforms, by contrast, the source is built from a purely geodesic trajectory. This is because the FD code uses the existence of discrete orbital frequencies. For this analysis, we specialize further to circular-orbit equatorial geodesics but allow these geodesics to evolve adiabatically using FD Teukolsky fluxes, as described in Ref. [63]. Previous work has shown that a self-consistent adiabatic evolution implemented with our FD code is in excellent agreement with the EOB model during the inspiral [29], and so it makes sense to compare TD and FD waveforms during this phase of the coalescence. It is also worth noting that FD waveforms can generally be computed to near machine accuracy using spectral techniques [64]. The only limitation on their accuracy is truncation of the (formally infinite) sums over multipoles and frequency harmonics. We can thus safely assume that the difference between TD and FD waveforms is only due to errors in the TD waves.

To perform this comparison, we align the $\ell = m = 2$ TD and FD waveforms by introducing time and phase shifts Δt and $\Delta\phi$ which minimize the gravitational phase difference at low frequencies. More specifically, we choose Δt and $\Delta\phi$ in order to minimize

$$\int_{t_1}^{t_2} [\phi_{22}^{\rm FD}(t) - \phi_{22}^{\rm TD}(t + \Delta t) + \Delta\phi]^2 {\rm d}t, \qquad (38)$$

where t_1 and t_2 are separated by $1000M$ and correspond to $M\omega_{22} \approx 0.108$ and a $M\omega_{22} \approx 0.111$, respectively. This low-frequency alignment is necessary for three reasons. First, the time coordinate of the TD waveform includes the effect of the extraction radii of the data used for the extrapolation; the FD waveforms are truly extracted at future null infinity. Second, the initial phases of the TD and FD trajectories are not necessarily the same, which introduces a phase offset between the two models. Third and last, as discussed in detail in Ref. [39], TD waveforms include an initial burst of "junk" radiation, which must be discarded. During that burst, the TD and FD trajectories may accumulate a small phase difference. We have found that small changes to t_1 and t_2 do not significantly affect the alignment.

Once Δt and $\Delta\phi$ are fixed, we have no freedom to introduce further time or phase shifts for the other modes. For instance, the difference between the FD and TD phases for the mode (ℓ, m) is

$$\delta\phi_{\ell m}^{\rm FD\text{-}TD} \equiv \left| \phi_{\ell m}^{\rm FD}(t) - \phi_{\ell m}^{\rm TD}(t + \Delta t) + m\frac{\Delta\phi}{2} \right|. \qquad (39)$$

The fractional amplitude difference is

$$\frac{\delta|h|_{\ell m}^{\rm FD\text{-}TD}}{|h|_{\ell m}} \equiv \left| \frac{|h|_{\ell m}^{\rm FD}(t)}{|h|_{\ell m}^{\rm TD}(t + \Delta t)} - 1 \right|. \qquad (40)$$

The Δt and $\Delta\phi$ used here are the ones that minimize (38).

Table I compares $\delta\phi_{\ell m}^{\rm FD\text{-}TD}$ and $\delta|h|_{\ell m}^{\rm FD\text{-}TD}/|h|_{\ell m}$ with the errors computed using the techniques described in Sec. III C. In particular, we examine the averages of $\delta\phi_{\ell m}^{\rm FD\text{-}TD}$ and $\delta|h|_{\ell m}^{\rm FD\text{-}TD}/|h|_{\ell m}$ over the alignment interval (t_1, t_2) and compare them to the averages over the same interval of the

TABLE I. The phase difference and fractional amplitude difference for various modes, averaged over the time interval $t_2 - t_1$ [see Eq. (38)]. We compare the amplitude and phase error found by comparing TD and FD waveforms (columns 2 and 4) with the TD errors we estimate using the techniques discussed in Sec. III C. In all cases but one [phase error for the (3, 2) mode], our numerical error estimates are larger than those we find comparing the two calculations; in that single discrepant case, the errors themselves are particularly small. This is further evidence that our numerical error estimates are reliable.

(ℓ, m)	$\delta\phi_{\ell m}^{\rm FD\text{-}TD}$	$\delta\phi_{\ell m}^{\rm TD}$	$\frac{\delta\lvert h\rvert_{\ell m}^{\rm FD\text{-}TD}}{\lvert h\rvert_{\ell m}}$	$\frac{\delta\lvert h\rvert_{\ell m}^{\rm TD}}{\lvert h\rvert_{\ell m}}$
(2, 2)	7.71×10^{-4}	1.27×10^{-3}	1.22×10^{-4}	8.20×10^{-4}
(3, 3)	1.18×10^{-3}	2.22×10^{-3}	1.95×10^{-4}	1.64×10^{-3}
(2, 1)	4.05×10^{-4}	1.28×10^{-3}	2.55×10^{-4}	1.03×10^{-3}
(4, 4)	1.58×10^{-3}	2.94×10^{-3}	2.80×10^{-4}	2.80×10^{-3}
(3, 2)	7.71×10^{-4}	3.92×10^{-4}	4.09×10^{-4}	3.13×10^{-3}

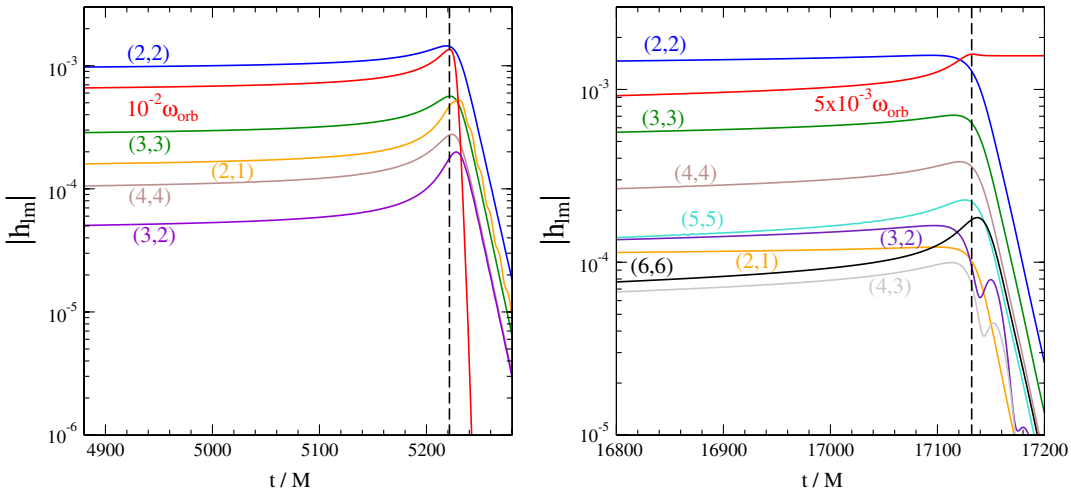

FIG. 3 (color online). Amplitude of the dominant modes during plunge, merger, and ringdown for $a = 0$ (left panel) and $a/M = 0.9$ (right panel). We also show orbital frequency, scaled to fit on the plot. As expected, the orbital frequency asymptotes to the horizon's angular velocity at late times because the frame dragging locks the particle's motion to that of the horizon. The vertical dashed line in the two panels marks the position of the peak of the orbital frequency.

TD numerical errors discussed in the previous section. For this comparison, we average the sum (in quadrature) of discretization and extrapolation errors. We see that the difference between TD and FD is always within the TD numerical errors, except for the $\ell = 3$, $m = 2$ mode. This mode is among the weakest of those that we show in Table I, which makes the extraction procedure described in the previous section considerably more difficult.

E. Characteristics of time-domain Teukolsky merger waveforms

We now turn to the waveforms produced by the TD Teukolsky analysis and their general characteristics. Figure 3 examines the behavior of the dominant TD modes $[(\ell, m) = (2, 2); (3, 3); (4, 4); (2, 1); (3, 2)]$ during plunge, merger and ringdown. We also show the orbital frequency of the EOB trajectory used to produce the TD data.

For the nonspinning case (left panel), the peak of the (2, 2) amplitude comes slightly earlier than the peak in orbital frequency, while higher-order modes peak later. A summary of the time difference $t^{\ell m}_{\rm peak} - t^{\Omega}_{\rm peak}$ between the peak of the Teukolsky mode amplitude and that of the EOB orbital frequency is shown in Table II. This difference can be as large as $6.25M$ for the (3, 2) mode, and even $8.82M$ for the (2, 1) mode.

The situation is different in the spinning case. A trend we see is that as the spin a grows positive, higher-order modes become progressively more important. In the right-hand panel of Fig. 3, we show the amplitude of the eight strongest modes for $a/M = 0.9$. As noticed in Ref. [54], modes with $\ell = m$ tend to increase more during the plunge. For example, the (5, 5) mode is smaller than the (3, 2) mode during inspiral but becomes larger during the plunge. The (6, 6) mode also grows quickly during the plunge (which roughly ends at the time of the peak of the orbital frequency). This behavior is not surprising; in fact, it should become more and more pronounced as the spin $a/M \to 1$; modes with large multipole moments become as important as low-ℓ modes in that limit, at least for quasicircular orbits [65,66].

Table III shows the time difference $(t^{22}_{\rm peak} - t^{\Omega}_{\rm peak})/M$ between the peak of the (2, 2) amplitude and of the orbital frequency for the values of spin that we consider in this paper. As the spin grows, the orbital frequency peaks later and later relative to the peak of the (2, 2) amplitude. This

TABLE II. The time difference $(t^{\ell m}_{\rm peak} - t^{\Omega}_{\rm peak})/M$ between the peak of the Teukolsky modes' amplitude and of the orbital frequency, for $a/M = 0$.

(ℓ, m)	$(t^{\ell m}_{\rm peak} - t^{\Omega}_{\rm peak})/M$
(2, 2)	−2.99
(3, 3)	0.52
(4, 4)	2.26
(2, 1)	8.82
(3, 2)	6.25

TABLE III. The time difference $(t^{22}_{\rm peak} - t^{\Omega}_{\rm peak})/M$ between the peak of the Teukolsky (2, 2) amplitude of the orbital frequency, for various values of the spin a/M. Also shown is the value of the orbital frequency at that peak, $M\Omega_{\rm max}$.

a/M	$(t^{22}_{\rm peak} - t^{\Omega}_{\rm peak})/M$	$M\Omega_{\rm max}$
−0.9	1.60	0.090
−0.5	−0.08	0.106
0	−2.99	0.136
0.5	−7.22	0.193
0.7	−12.77	0.236
0.9	−39.09	0.320

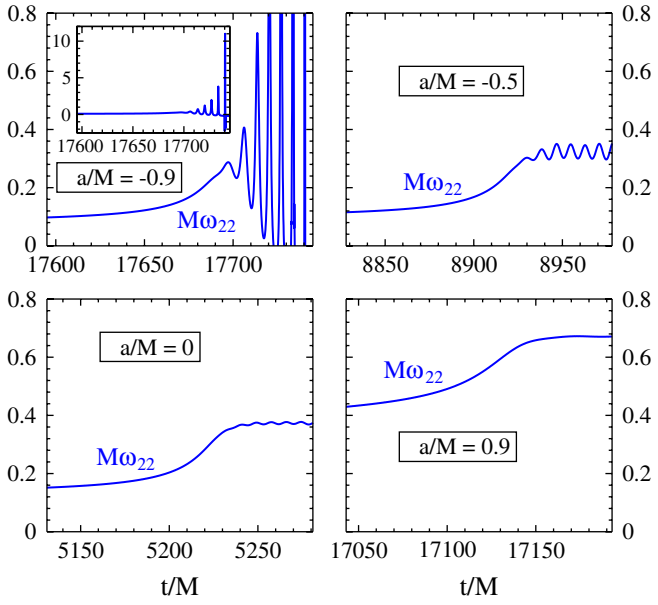

FIG. 4 (color online). The evolution of wave frequency for the (2, 2) mode for several spins. Notice that the strong late oscillations (during ringdown), which are particularly prominent as the spin decreases towards negative values; they are especially large for $a/M = -0.9$. These oscillations are physical and arise from superposition of the $(2, \pm 2)$ QNMs.

has important implications for modeling the EOB merger-ringdown waveform, as we discuss in detail later in the paper.

Another interesting feature of the Teukolsky waveforms that we find is shown in Fig. 4. This figure shows the gravitational-wave frequency (defined as the time derivative of the phase) for the (2, 2) mode during plunge, merger, and ringdown, for several spin values. Notice the strong oscillations seen at late times (during the final ringdown) for spins $a \lesssim 0$. These oscillations grow as the spin decreases and become very large for $a/M = -0.9$. We have verified that these oscillations (even in the $a/M = -0.9$ case) are *not* numerical artifacts. We have found that they are insensitive to numerical resolution and floating-point precision, that they also appear in the context of other plunging retrograde trajectories. We find that they are due to a superposition of the dominant (2, 2) QNM with the $(2, -2)$ QNM, which is also excited during the plunge [34,56].

In order to extract the relative amplitudes of these modes, we fit the gravitational-wave frequency in a region where the higher overtones of the $(2, \pm 2)$ modes have decayed away and the waveform can be described by

$$h(t) = h_0(e^{-i\sigma_{220}t} + \bar{\alpha}e^{i\sigma^*_{2-20}t+\bar{\beta}}), \tag{41}$$

where $\sigma_{2\pm20} = \omega_{2\pm20} - i/\tau_{2\pm20}$ are the complex QNM frequencies [with overtone $n = 0$, as introduced in Eq. (18)]. The complex parameter h_0 and real parameters $\bar{\alpha}$, $\bar{\beta}$ are left unspecified. From Eq. (41) one can then calculate the frequency as $\Re[-i\dot{h}(t)/h(t)]$. Because h_0 cancels in this expression, we are left with the parameters $\bar{\alpha}$ and $\bar{\beta}$, which can be determined by numerical fitting [34]. We find that the relative excitation $\bar{\alpha}$ of the $(2, -2)$ modes goes from $\bar{\alpha} \approx 0.005$ for $a/M = 0$ to $\bar{\alpha} \approx 0.03$ for $a/M = -0.5$ and $\bar{\alpha} \approx 0.46$ for $a/M = -0.9$. This is nicely in accord with the growing strength of the oscillations as $a/M \to -1$ that is seen in Fig. 4.

A possible reason why the $(2, -2)$ QNM is strongly excited for large negative spins can be understood by examining the particle's trajectory. When $a < 0$, the spin angular momentum is oppositely directed from the orbital angular momentum. During the inspiral, when the orbit is very wide, the orbit's angular velocity is opposite to the sense in which the horizon rotates. At late times (during the final plunge), the particle's motion becomes locked to the horizon by frame dragging. The particle's angular velocity thus flips sign at some point during the plunge when $a < 0$. This change in angular velocity is most pronounced for large negative spins, since the difference between the frequency at the innermost stable circular orbit (ISCO) and at the event horizon is largest for large negative a.

Figure 5 shows, as an example, the EOB trajectory we used to produce the $a/M = -0.9$ Teukolsky waveforms. As viewed here, the horizon rotates in the clockwise sense. After the anticlockwise inspiral, the particle plunges and its angular velocity flips sign before the particles settles on a quasi-circular orbit with $r \to r_+$ and $\Omega \to \Omega_+ = a/2Mr_+$ as $t \to +\infty$ (where $r_+ = M + \sqrt{M^2 - a^2}$ is the coordinate radius of the event horizon). This behavior leads us to conjecture that the $(2, -2)$ QNM is excited by the last part of the plunge, when the particle is corotating with the black hole.

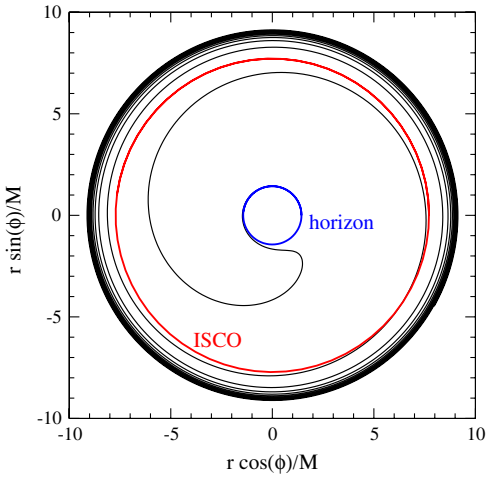

FIG. 5 (color online). The EOB equatorial orbit used to produce the Teukolsky waveforms for $a/M = -0.9$, focusing on the transition between the inspiral and the plunge. As shown here, the Kerr black hole rotates clockwise. The red external circle is the ISCO; the blue internal one is the event horizon. The particle initially moves anticlockwise on quasicircular orbits but flips to clockwise motion during the plunge as its angular motion becomes locked to the horizon's motion.

The (2, 2) QNM is excited by the final inspiral and initial plunge, when the particle is counter-rotating relative to the black hole. When $a > 0$ the particle's motion is always corotating with the black hole, both during inspiral and through the plunge. This conjecture thus explains why oscillations in the ringdown frequency are much less significant for $a \gtrsim 0$ and seem to disappear when $a/M \approx 1$ (see Fig. 4).

IV. COMPARISON OF THE EOB MODEL WITH THE TEUKOLSKY TIME-DOMAIN WAVEFORMS

In this Section, we present the main results of this paper, comparing the EOB waveforms for binary coalescence with waveforms calculated using the time-domain Teukolsky-equation tools described in the previous section. We begin by comparing Teukolsky waveforms (for $a = 0$) with an EOB model that has been calibrated for the comparable-mass case (Sec. IV A). The agreement is good for some modes [(2, 2) and (3, 3)] but is much less good for others [(2, 1) and (4, 4)]. We nail down the reason for this disagreement, recalibrate the EOB model, and show much better agreement in the comparison in Sec. IV B. We then consider $a \neq 0$. Focusing on the (2, 2) mode, we compare Teukolsky and EOB waveforms for a range of spins in Sec. IV C.

We stress that all the comparisons that we present in this paper have been performed between EOB and Teukolsky waveforms produced with the *same* EOB trajectory. For example, in order to recalibrate the EOB model, we start with a reasonable EOB trajectory; we feed that to the Teukolsky code and compare the resulting Teukolsky waveforms to the EOB waveforms. If the waveforms do not agree, we modify the EOB trajectory so that the EOB waveforms agree with the Teukolsky waveforms produced with the old EOB trajectory and then feed the new EOB trajectory to the Teukolsky code. We then iterate until this procedure has converged.

A. Comparison of comparable-mass EOB waveforms and Teukolsky waveforms for $a=0$

Reference [28] presents an EOB model calibrated to numerical-relativity simulations of nonspinning black-hole binaries with mass ratios $m_2/m_1 = 1,\ 1/2,\ 1/3,\ 1/4$, and $1/6$. This model achieves very good agreement between the phase and amplitude of the EOB and numerical-relativity waveforms; see Secs. II and III of Ref. [28] for details. As background for the comparison we will make to the Teukolsky waveform, we briefly discuss how the EOB inspiral-plunge waveform was built and how the merger-ringdown waveform was attached to build the full waveform

For each mode, Ref. [28] set $a_4^{h_{\ell m}} = a_5^{h_{\ell m}} = b_3^{h_{\ell m}} = 0$ in Eq. (17) and fixed the remaining coefficients $a_i^{h_{\ell m}}$ $[i \in (1, 2, 3)]$ and $b_i^{h_{\ell m}}$ $[i \in (1, 2)]$ by imposing the following five conditions:

(1) The time at which the EOB h_{22} reaches its peak should coincide with the time at which the EOB orbital frequency Ω reaches its peak. We denote this time with $t^{\Omega}_{\rm peak}$. The peaks of higher-order numerical modes differ from the peak of the numerical h_{22}; we define this time difference as

$$\Delta t^{\ell m}_{\rm peak} = t^{\ell m}_{\rm peak} - t^{22}_{\rm peak} = t_{d|h^{\rm NR}_{\ell m}|/dt=0} - t_{d|h^{\rm NR}_{22}|/dt=0}. \quad (42)$$

We require that the peaks of the EOB $h_{\ell m}$ occur at the time $t^{\Omega}_{\rm peak} + \Delta t^{\ell m}_{\rm peak}$:

$$\left.\frac{d|h^{\rm EOB}_{\ell m}|}{dt}\right|_{t^{\Omega}_{\rm peak}+\Delta t^{\ell m}_{\rm peak}} = 0. \quad (43)$$

(2) The peak of the EOB $h_{\ell m}$ should have the same amplitude as the peak of the numerical $h_{\ell m}$:

$$|h^{\rm EOB}_{\ell m}(t^{\Omega}_{\rm peak} + \Delta t^{\ell m}_{\rm peak})| = |h^{\rm NR}_{\ell m}(t^{\ell m}_{\rm peak})|. \quad (44)$$

(3) The peak of the EOB $h_{\ell m}$ should have the same second time derivative as the peak of the numerical $h_{\ell m}$:

$$\left.\frac{d^2|h^{\rm EOB}_{\ell m}|}{dt^2}\right|_{t^{\Omega}_{\rm peak}+\Delta t^{\ell m}_{\rm peak}} = \left.\frac{d^2|h^{\rm NR}_{\ell m}|}{dt^2}\right|_{t^{\ell m}_{\rm peak}}. \quad (45)$$

(4) The frequency of the numerical and EOB $h_{\ell m}$ waveforms should coincide at their peaks:

$$\omega^{\rm EOB}_{\ell m}(t^{\Omega}_{\rm peak} + \Delta t^{\ell m}_{\rm peak}) = \omega^{\rm NR}_{\ell m}(t^{\ell m}_{\rm peak}). \quad (46)$$

(5) The time derivative of the frequency of the numerical and EOB $h_{\ell m}$ waveforms should coincide at their peaks:

$$\dot{\omega}^{\rm EOB}_{\ell m}(t^{\Omega}_{\rm peak} + \Delta t^{\ell m}_{\rm peak}) = \dot{\omega}^{\rm NR}_{\ell m}(t^{\ell m}_{\rm peak}). \quad (47)$$

[Note that the quantities $h^{\rm EOB}_{\ell m}$ referenced in the above equations are the same as the quantities $h^{\rm insp\text{-}plunge}_{\ell m}$ defined in Eq. (10).]

The functions $\Delta t^{\ell m}_{\rm peak}$, $|h^{\rm NR}_{\ell m}(t^{\ell m}_{\rm peak})|$, $d^2|h^{\rm NR}_{\ell m}|/dt^2|_{t^{\ell m}_{\rm peak}}$, $\omega^{\rm NR}_{\ell m}(t^{\ell m}_{\rm peak})$, and $\dot{\omega}^{\rm NR}_{\ell m}(t^{\ell m}_{\rm peak})$ described in Ref. [28] were extracted from numerical-relativity and Teukolsky data, and approximated by smooth functions of the symmetric mass ratio ν. Least-square fits for these quantities were given in Table III of Ref. [28]. These fits included information about the $\nu = 10^{-3}$ case from the analysis of this paper (which was in preparation as Ref. [28] was completed).

Since $|h_{\ell m}(t^{\ell m}_{\rm peak})|$ and $d^2|h_{\ell m}|/dt^2|_{t^{\ell m}_{\rm peak}}$ approach zero in the test-particle limit, their input values at $\nu = 10^{-3}$ do not affect the least-square fits very much. For the (2, 2) and (3, 3) modes, the data points are very regular. This is illustrated for the (2, 2) case in Fig. 6. The residues of

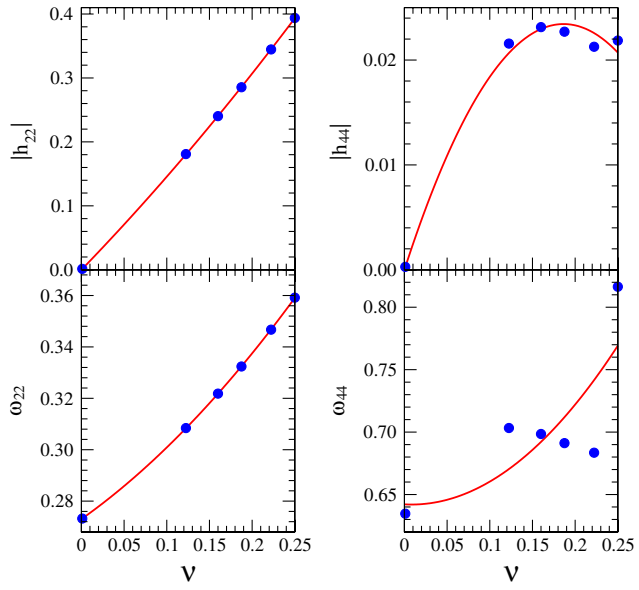

FIG. 6 (color online). The amplitude h (top panels) and gravitational-wave frequency ω (bottom panels) when the (2, 2) (left) and (4, 4) (right) modes reach their peak. Circles at $\nu \geq 0.12$ denote data points extracted from the numerical-relativity simulations; the left-most points at $\nu = 10^{-3}$ are data extracted with the Teukolsky code. The solid lines are quadratic fits to the data points.

the fit at $\nu = 10^{-3}$ are very small, and the ν fits agree well with the values from the Teukolsky code at $\nu = 10^{-3}$. Unfortunately, this is not the case for the (2, 1) and (4, 4) modes. Figure 6 shows this for the (4, 4) mode. The $|h_{44}(t^{44}_{\rm peak})|$ data points do not lie on a smooth curve, and so the fit is intrinsically unstable. By minimizing the relative residue instead of the absolute residue in the least-square fit, we increase the weight on the $\nu = 10^{-3}$ data point and get a much better fit at low mass ratio, but at the cost of a much poorer fit in the comparable-mass regime. The situation is even worse for $\omega_{44}(t^{44}_{\rm peak})$, for which the data points for comparable masses have a rather irregular trend. These results emphasize the need for more accurate numerical-relativity data describing the higher-order modes in order to smoothly connect these quantities from the test-particle limit to the equal-mass case.

Once the coefficients $a_i^{h_{\ell m}}$ and $b_i^{h_{\ell m}}$ are known, we calculate $h^{\rm insp\text{-}plunge}_{\ell m}$ using Eq. (10) and attach the QNMs using Eq. (19). We assume the following comb widths [28],

$$\Delta t^{22}_{\rm match} = 5M, \qquad \Delta t^{33}_{\rm match} = 12M, \tag{48a}$$

$$\Delta t^{44}_{\rm match} = 9M, \qquad \Delta t^{21}_{\rm match} = 8M, \tag{48b}$$

and choose $t^{\ell m}_{\rm match} = t^{\Omega}_{\rm peak} + \Delta t^{\ell m}_{\rm peak}$ with $\Delta t^{\ell m}_{\rm peak}$ given in Eq. (42). It was found in Ref. [28] that, after calibrating the EOB adjustable parameters and aligning the EOB and numerical waveforms at low frequency, the difference between $t^{22}_{\rm peak}$ and $t^{\Omega}_{\rm peak}$ is typically $\sim 1M$. Thus, Ref. [28] assumed that $t^{\Omega}_{\rm peak} = t^{22}_{\rm peak}$ and consequently set $\Delta t^{22}_{\rm peak} = 0$. Following these findings, we attach the QNMs at $t^{\Omega}_{\rm peak}$ for the (2, 2) mode and at $t^{\Omega}_{\rm peak} + \Delta t^{\ell m}_{\rm peak}$ for all the other modes.

Figures 7 and 8 compare the leading modes generated by this EOB model with the modes generated by the time-domain Teukolsky code. We adopt the waveform alignment procedure used in Refs. [21,22,28,54] and Sec. III D, aligning the waveforms at low-frequency by minimizing

$$\int_{t_1}^{t_2} [\phi_1(t) - \phi_2(t - \Delta t) - \Delta\phi]^2 dt, \tag{49}$$

over a time shift Δt and a phase shift $\Delta\phi$. Here, $\phi_1(t)$ and $\phi_2(t)$ are the gravitational phases of the EOB and Teukolsky h_{22}. We chose $t_2 - t_1 = 1000M$ and center these times when the orbital frequencies are low. We have verified that our results are insensitive to the precise location of this integration interval, provided that it is chosen during the inspiral phase.

As expected from the discussion above, Fig. 7 shows that there is quite good agreement between the EOB and Teukolsky models for the (2, 2) and (3, 3) modes. In

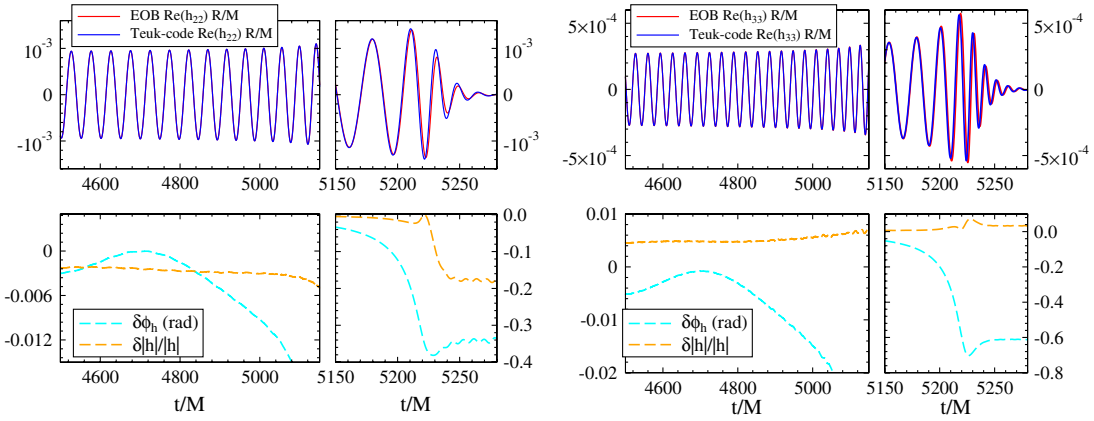

FIG. 7 (color online). Comparison between (2, 2) and (3, 3) modes generated by the Teukolsky code for $a = 0$, and the corresponding modes produced with the EOB model of Ref. [28]. The EOB model was calibrated to numerical-relativity simulations at mass ratios 1, 1/2, 1/3, 1/4, 1/6 and extrapolated to $\nu = 10^{-3}$. Upper panels show the real part of the modes; lower panels show the phase and fractional amplitude differences.

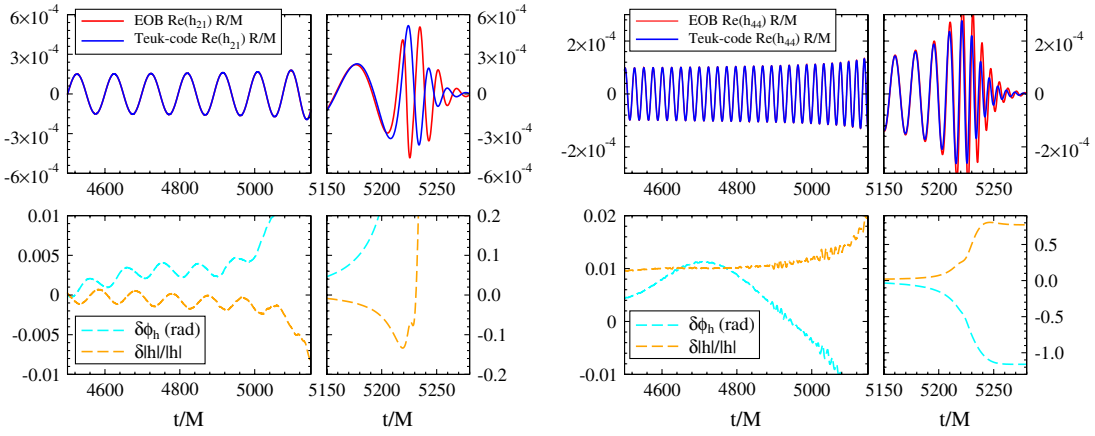

FIG. 8 (color online). The same as Fig. 7 but for the (2, 1) and (4, 4) modes.

particular, the difference in both the amplitude and the phase is quite small until the inspiral reaches the ISCO. This excellent agreement is due to the resummed-factorized energy flux [13] employed in the EOB equations of motion and waveforms (see previous studies [15,32–36,67,68]). The amplitude disagreement during merger and ringdown is due to our procedure of attaching QNMs to the EOB waveform [see Fig. 3 and discussion around in Ref. [28]]. The accumulation of some phase difference during plunge will be discussed at the end of this section.

Figure 8 shows that the agreement between the EOB and Teukolsky (2, 1) and (4, 4) modes remains excellent during the long inspiral but is not very satisfactory during the merger and ringdown. For the (4, 4) mode, the EOB amplitude becomes too large toward merger. This is a consequence of the excessively large residue of the ν fit for $|h_{44}(t^{44}_{\rm peak})|$ at $\nu = 10^{-3}$. For the (2, 1) mode, the EOB model of Ref. [28] fails to reproduce a reasonable merger waveform. This problem is related to the fact that the value of $\Delta t^{21}_{\rm peak}$ at $\nu = 10^{-3}$ used in Ref. [28] to determine the ν fit is too large (see Table II). The problem is deeper than this, however. In particular, the value is uncertain due to the (unusual) broadness of the Teukolsky (2, 1) mode's peak (see Fig. 3). We shall see in the next section that to improve the agreement of the (2, 1) mode, we need a smaller value for $\Delta t^{21}_{\rm peak}$.

An additional source of error arises from the procedure that was used to compute the NQC coefficients $a_1^{h_{22}}$, $a_2^{h_{22}}$, and $a_3^{h_{22}}$ used in N_{22} [see Eq. (17)]. In Ref. [28], these coefficients were calculated by an iterative procedure using the five conditions discussed at the beginning of this section. These coefficients have small but non-negligible effects on the EOB dynamics: through the amplitude $|h_{22}|$, they enter the energy flux [see Eq. (9)] and thereby influence the rate at which the small body spirals in.[3] This iterative procedure increases by a factor of a few the computational cost of generating h_{22}. To mitigate this cost increase, Ref. [28] suggested replacing the iterative procedure with ν fits for $a_1^{h_{22}}$, $a_2^{h_{22}}$, and $a_3^{h_{22}}$. These fits were obtained using data for mass ratios 1, 1/2, 1/3, 1/4, and 1/6. The EOB waveforms shown in Figs. 7 and 8 are then generated using these ν fits extrapolated to $\nu = 10^{-3}$. When comparing the fit and the true values of $a_1^{h_{22}}$, $a_2^{h_{22}}$, and $a_3^{h_{22}}$ at $\nu = 10^{-3}$, we find a non-negligible difference which is responsible for $\sim$0.4 rad difference between the EOB and Teukolsky (2, 2) modes and for $\sim$0.6 rad difference for the (3, 3) modes. In the next section, we shall show that by returning to the iterative procedure, rather than using the fits, we can do much better.

Lastly, we comment on why for the (2, 1) and (4, 4) modes in Eq. (13b) we replaced $v_\Phi^{(\ell+\epsilon)}$ with $v_\Phi^{(\ell+\epsilon-2)}/r_\Omega$. As discussed above, the amplitude of the numerical (2, 1) and (4, 4) modes reaches a peak a fairly long time after the peak of the (2, 2) mode. Thus, in order to impose the first condition (in our list of five) given above, the peak of the EOB mode should be moved to $t^\Omega_{\rm peak} + \Delta t^{\ell m}_{\rm peak}$. However, the leading EOB amplitude is proportional to a power of the orbital frequency. This frequency decreases to zero at the horizon, and so the EOB amplitude drops to an extremely small value at $t^\Omega_{\rm peak} + \Delta t^{\ell m}_{\rm peak}$. By replacing $v_\Phi^2 = (M r_\Omega \Omega)^2$ with $1/r_\Omega$, we slow the decay of these modes after $t^\Omega_{\rm peak}$ and can successfully move the peak of the mode to $t^\Omega_{\rm peak} + \Delta t^{\ell m}_{\rm peak}$. This modification was also adopted in Ref. [28] to successfully model the (2, 1) and (4, 4) modes in the comparable-mass case.

B. Comparison of calibrated EOB waveforms and Teukolsky waveforms for $a=0$

We now improve on the EOB model of Ref. [28] to more accurately reproduce Teukolsky waveforms. We focus on comparisons for the $a = 0$ limit, although we discuss how we build our model for general spins. We start from the five conditions discussed at the beginning of Sec. IV A which allow us to compute the NQC coefficients:

[3]Note that the NQC coefficients $a_i^{h_{\ell m}}$ of higher-order modes contribute much less to the energy flux and can be safely ignored in the dynamics of comparable-mass binaries [28].

$$\left.\frac{d|h^{\rm EOB}_{\ell m}|}{dt}\right|_{t^{\Omega}_{\rm peak}+\Delta t^{\ell m}_{\rm peak}} = 0 \tag{50}$$

$$|h^{\rm EOB}_{\ell m}(t^{\Omega}_{\rm peak}+\Delta t^{\ell m}_{\rm peak})| = |h^{\rm Teuk}_{\ell m}(t^{\ell m}_{\rm peak})|, \tag{51}$$

$$\left.\frac{d^2|h^{\rm EOB}_{\ell m}|}{dt^2}\right|_{t^{\Omega}_{\rm peak}+\Delta t^{\ell m}_{\rm peak}} = \left.\frac{d^2|h^{\rm Teuk}_{\ell m}|}{dt^2}\right|_{t^{\ell m}_{\rm peak}}, \tag{52}$$

$$\omega^{\rm EOB}_{\ell m}(t^{\Omega}_{\rm peak}+\Delta t^{\ell m}_{\rm peak}) = \omega^{\rm Teuk}_{\ell m}(t^{\ell m}_{\rm peak}), \tag{53}$$

$$\dot{\omega}^{\rm EOB}_{\ell m}(t^{\Omega}_{\rm peak}+\Delta t^{\ell m}_{\rm peak}) = \dot{\omega}^{\rm Teuk}_{\ell m}(t^{\ell m}_{\rm peak}), \tag{54}$$

where

$$\Delta t^{\ell m}_{\rm peak} = t^{\ell m}_{\rm peak} - t^{\Omega}_{\rm peak} = t_{d|h^{\rm Teuk}_{\ell m}|/dt=0} - t_{d\Omega/dt=0}. \tag{55}$$

As before, the quantities $h^{\rm EOB}_{\ell m}$ given above are equivalent to the quantities $h^{\rm insp\text{-}plunge}_{\ell m}$ in Eq. (10). The quantities on the RHSs of Eqs. (50)–(54) are now computed from the Teukolsky waveforms, rather than using the ν fits of Ref. [28], as in Sec. IV A. Notice that $\Delta t^{\ell m}_{\rm peak}$ in Eq. (55) differs from the one in Eq. (42). In fact, since the Teukolsky code uses the EOB trajectory, the time difference between the peak of any (ℓ, m) mode and the peak of the orbital frequency is unambiguous. This was not the case in Ref. [28] where numerical-relativity waveforms are used. In that case, the time difference between the peak of the numerical-relativity (ℓ, m) modes and the peak of the EOB orbital frequency depends on the alignment procedure between the numerical and EOB waveforms and on the calibration of the EOB adjustable parameters. This is why Ref. [28] adopted the $\Delta t^{\ell m}_{\rm peak}$ described in Eq. (42).

As discussed in Sec. IV A, Ref. [28] assumed that $t^{\Omega}_{\rm peak} = t^{22}_{\rm peak}$ and consequently set $\Delta t^{22}_{\rm peak} = 0$. However, as seen in Tables II and III, the Teukolsky data show that $t^{\Omega}_{\rm peak} - t^{22}_{\rm peak}$ differs from zero when $\nu = 10^{-3}$; this effect is particularly pronounced for large positive Kerr spin parameters. The modified prescription given by Eq. (55) is thus quite natural. By contrast, the prescription described in Ref. [28] is bound to fail for all the modes in the test-particle limit. We point out that in Appendix A of Ref. [35] the authors explored how nonspinning waveforms can be improved by attaching the QNMs at a shifted time (common to all modes) $\sim 3M$ past the peak of the orbital frequency, while maintaining the determination of the NQC parameters at the peak of the orbital frequency.

In the nonspinning case, we solve Eqs. (50) and (51) for $a^{h_{\ell m}}_i$ with $i = 1, 2, 3$ and set $a^{h_{\ell m}}_4 = a^{h_{\ell m}}_5 = 0$. In the spinning case, in order to not introduce spin-dependence at leading order, we fix $a^{h_{\ell m}}_1$ and $a^{h_{\ell m}}_2$ to the values calculated for $a = 0$ and solve for $a^{h_{\ell m}}_i$ (with $i = 3, 4, 5$). As for the phase NQC coefficients, in the nonspinning case we solve Eqs. (52) and (53) for $b^{h_{\ell m}}_i$ (with $i = 1, 2$) and set $b^{h_{\ell m}}_3 = b^{h_{\ell m}}_4 = 0$. In the spinning case, we fix $b^{h_{\ell m}}_1$ and $b^{h_{\ell m}}_2$ to their $a = 0$ values (again, in order to not introduce any spin-dependence at leading order) and solve for $b^{h_{\ell m}}_3$ and $b^{h_{\ell m}}_4$.

Once the coefficients $a^{h_{\ell m}}_i$ and $b^{h_{\ell m}}_i$ are known, we calculate $h^{\rm insp\text{-}plunge}_{\ell m}$ using Eq. (10) and attach the QNMs using Eq. (19), assuming the comb's width as in Eq. (48). Furthermore, we choose $t^{\ell m}_{\rm match} = t^{\Omega}_{\rm peak} + \Delta t^{\ell m}_{\rm peak}$ with $\Delta t^{\ell m}_{\rm peak}$ given in Eq. (55). The merger-ringdown (2, 2) mode is now attached at the time where the Teukolsky (2, 2) amplitude peaks, in contrast to the approach used in Ref. [28]. All the other merger-ringdown (ℓ, m) modes are attached at the time the corresponding Teukolsky (ℓ, m) amplitudes peaks, which is the same procedure followed in Ref. [28].

Figures 9 and 10 compare these calibrated EOB models to the Teukolsky amplitudes. Table IV lists the input parameters used on the RHSs of Eqs. (50)–(54). We emphasize that the value of $\Delta t^{21}_{\rm peak}$ we reported in this table and

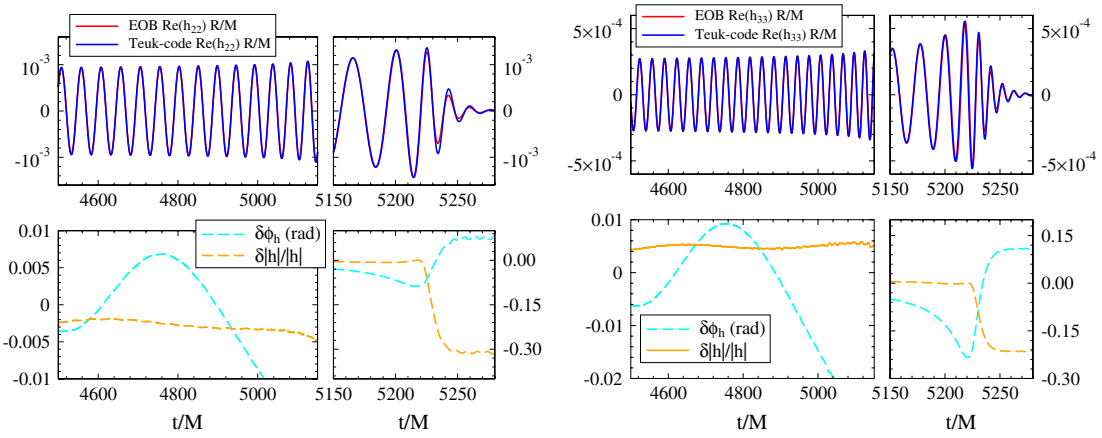

FIG. 9 (color online). The same as Fig. 7 but for the Teukolsky-calibrated EOB model described in Sec. IV B.

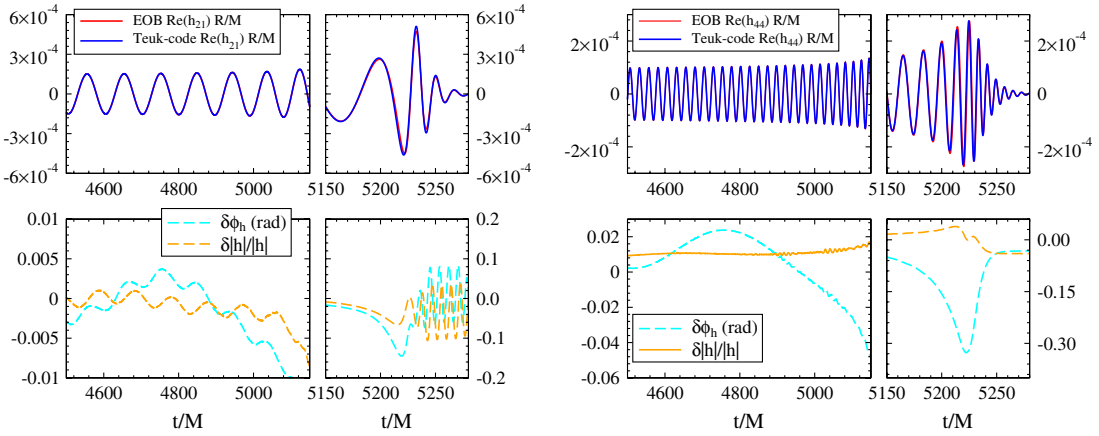

FIG. 10 (color online). The same as Fig. 8 but for the Teukolsky-calibrated EOB model described in Sec. IV B.

that we use in our model is $2.5M$ smaller than the difference $t^{21}_{\rm peak} - t^{\Omega}_{\rm peak}$. We do this because the peak of the Teukolsky (2, 1) amplitude is quite broad, and at the time $t^{21}_{\rm peak}$ where the peak occurs the Teukolsky mode's frequency oscillates due to superposition of the $\ell = 2$, $m \pm 1$ modes, as discussed in Sec. III E. (See also Ref. [34] and Fig. 3 of Ref. [35], which shows similar oscillations.) Although these oscillations are physical, we do not attempt to reproduce them in our EOB waveform, as their effect on the phase agreement between the EOB and Teukolsky waveforms is negligible. We therefore simply choose a slightly smaller value of $\Delta t^{21}_{\rm peak}$, ensuring that $t^{\Omega}_{\rm peak} + \Delta t^{21}_{\rm peak}$ is within the broad peak of $h^{21}_{\rm peak}$. This in turn ensures that the oscillations in frequency do not impact our results.

Figure 10 demonstrates that, by calibrating against the Teukolsky waveforms using the input values shown in Table IV, the agreement between the EOB and Teukolsky waveforms is considerably improved during merger and ringdown for the (2, 1) and (4, 4) modes. Improvements to the (2, 2) and (3, 3) modes (Fig. 9) are less significant, since the model of Ref. [28] works quite well for these modes. As we discussed in the previous section, the input parameters listed in Table IV are well predicted by the fitting formulas of Ref. [28] (see also Fig. 6). There is, however, noticeable improvement in phase agreement between Figs. 7 and 9. This is due to the fact that in the latter case we use the iterative procedure to compute the NQC coefficients a_i, as discussed at the end of Sec. IV A.

TABLE IV. Input values for the RHSs of Eqs. (50)–(54) for the EOB model for nonspinning black holes used in Figs. 9 and 10.

(ℓ, m)	$\Delta t^{\ell m}_{\rm peak}$	$\lvert h^{\rm Teuk}_{\ell m,{\rm peak}}\rvert$	$d^2\lvert h^{\rm Teuk}_{\ell m,{\rm peak}}\rvert/dt^2$	$\omega^{\rm Teuk}_{\ell m,{\rm peak}}$	$\dot\omega^{\rm Teuk}_{\ell m,{\rm peak}}$
(2, 2)	−2.99	0.001450	-3.171×10^{-6}	0.2732	0.005831
(2, 1)	6.32	0.0005199	-7.622×10^{-7}	0.2756	0.01096
(3, 3)	0.52	0.0005662	-1.983×10^{-6}	0.4546	0.01092
(4, 4)	2.26	0.0002767	-1.213×10^{-6}	0.6347	0.01547

Comparing to the discussion of numerical error in Sec. III C, we note that the differences in phase and amplitude between the EOB and Teukolsky modes shown in Figs. 9 and 10 are within the numerical errors essentially through the plunge; the differences grow larger than these errors during merger and ringdown. As this analysis was being completed, we acquired the capability to produce Teukolsky waveforms using the hyperboloidal layer method (Ref. [53]; see also Ref. [36]). We have compared phase and amplitude differences for the (2, 2) mode between the Teukolsky code used for the bulk of this analysis and the hyperboloidal variant. We have found that these differences are within the errors discussed in Sec. III C.

C. Comparisons for general spin

We conclude our discussion of results by comparing, for the first time, EOB and Teukolsky coalescence waveforms with $a \neq 0$. These waveforms are produced using the trajectory of the spinning EOB model described in Sec. II. As in the nonspinning case, understanding the transition from inspiral to ringdown in the test-particle limit when the central black hole carries spin can help modeling the plunge-merger waveforms from comparable-mass spinning black holes.

As in the nonspinning case [15,32–36,67,68], we expect that the resummed-factorized energy-flux and mode amplitudes agree quite well with the Teukolsky data at least up to the ISCO, provided that the spin is not too high. In fact, Ref. [15] showed that, in the adiabatic limit, the resummed-factorized (2, 2) modes agree very well with frequency-domain Teukolsky modes up to the ISCO, at least over the range $-1 \leq a/M \lesssim 0.7$. The relative difference between amplitudes in the two models is less than 0.5% when $a/M \leq 0.5$ but grows to 3.5% when $a/M \simeq 0.75$.

In this work, we focus on the (2, 2) mode comparison, leaving to a future publication a thorough study of the higher modes. We have already seen in Sec. III E that as

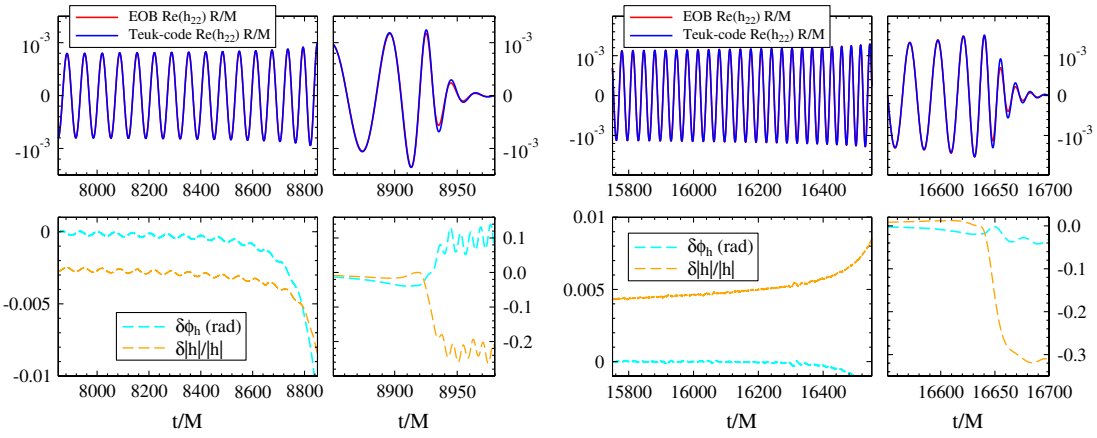

FIG. 11 (color online). Comparison of Teukolsky-calibrated EOB and Teukolsky (2, 2) modes for $a/M = -0.5$ (left panel) or $a/M = 0.5$ (right panel). Upper panels show the real part of the modes; lower panels show phase and fractional amplitude differences.

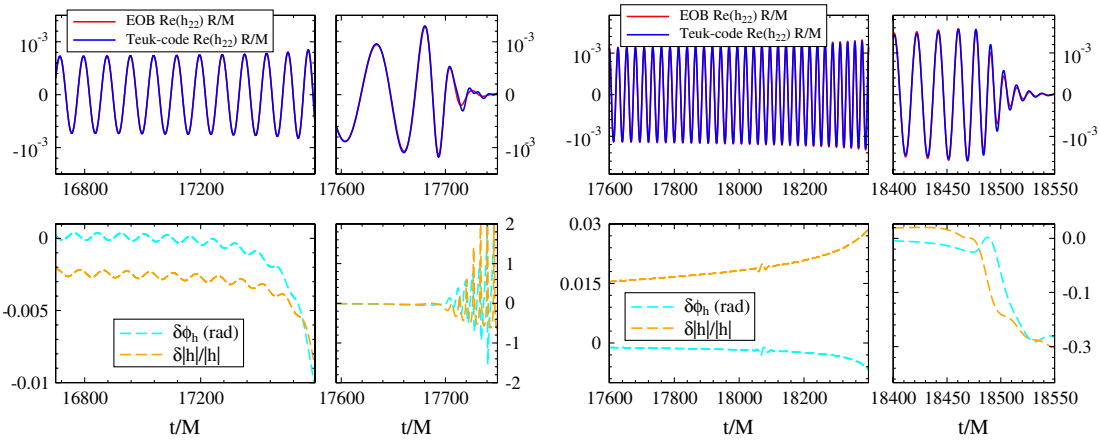

FIG. 12 (color online). The same as Fig. 11 but for $a/M = -0.9$ (left panel) and $a/M = 0.7$ (right panel).

$a/M \to 1$, many more modes become excited during the plunge and merger. For this limit, the resummed-factorized waveforms will need to be improved in order to match higher-order Teukolsky modes with good precision.

Figs. 11 and 12 compare (2, 2) modes for the EOB and Teukolsky waves for spin values $a/M = \pm 0.5$, $a/M = 0.7$, and $a/M = -0.9$. We build the full EOB waveform following the prescription described in Sec. IV B, using the input parameters shown in Table V. For the cases $a/M = 0.5$ and $a/M = 0.7$, we also use a *pseudo* QNM (pQNM) (in addition to the *standard* QNMs) as suggested in Refs. [22,28]. A possible physical motivation of these pQNMs follows. The peak of the orbital frequency comes from orbits that are very close to the light-ring position [14], which in turn corresponds nearly to the peak of the effective potential for gravitational perturbations [69–73]. Therefore, before the orbital frequency peaks, the gravitational-wave emission is dominated by the source of the Teukolsky equations (i.e. by the particle); afterwards, the emission is dominated by the black-hole's QNMs. In the standard EOB approach, the waveform is a superposition of QNMs already after the peak of the numerical amplitude $t^{\ell m}_{\rm peak}$. However, we have seen that this precedes the peak of the orbital frequency by a considerable time interval: $-\Delta t_{\ell m} \approx 12$–$40M$ for $a/M = 0.5$ and $a/M = 0.7$ (see Table V). To account

TABLE V. Input values for the RHSs of Eqs. (50)–(54) for the EOB (2, 2) mode for spinning black holes used in Figs. 11 ($a/M = \pm 0.5$) and 12 ($a/M = 0.7$ and $a/M = -0.9$). We also include data for the case $a/M = 0.9$, although we do not compare waveforms for this example.

a/M	$\Delta t^{22}_{\rm peak}$	$\lvert h^{\rm Teuk}_{22,\rm peak}\rvert$	$d^2\lvert h^{\rm Teuk}_{22,\rm peak}\rvert/dt^2$	$\omega^{\rm Teuk}_{22,\rm peak}$	$\dot{\omega}^{\rm Teuk}_{22,\rm peak}$
-0.9	1.60	0.001341	-3.532×10^{-6}	0.2195	0.005676
-0.5	-0.08	0.001382	-2.536×10^{-6}	0.2376	0.006112
0.5	-7.22	0.001542	-1.334×10^{-6}	0.3396	0.005095
0.7	-12.77	0.001582	-1.212×10^{-6}	0.3883	0.004068
0.9	-39.09	0.001576	-8.102×10^{-8}	0.4790	0.001779

TABLE VI. The time delay $\Delta t^{21}_{\rm peak}$, $\Delta t^{33}_{\rm peak}$, and $\Delta t^{44}_{\rm peak}$ defined in Eq. (55) for $a/M = -0.9$, -0.5, 0.5, 0.7, and 0.9. Time delay information for the nonspinning case $a/M = 0$ and the dominant (2, 2) mode are given in Tables II and III.

a/M	$\Delta t^{21}_{\rm peak}$	$\Delta t^{33}_{\rm peak}$	$\Delta t^{44}_{\rm peak}$
−0.9	14.26	3.81	5.41
−0.5	12.63	2.71	4.36
0.5	3.87	−1.99	0.28
0.7	0.10	−5.02	−2.16
0.9	−34.48	−17.57	−11.80

for the effect of the particle emission before the peak of the orbital frequency, we therefore introduce a pQNM having frequency $\omega^{\rm pQNM}_{22} = 2\Omega_{\rm max}$ (cf. Table III) and decay time $\tau^{\rm pQNM}_{22} = -\Delta t^{22}_{\rm peak}/2$. We included this pQNM only for $a/M = 0.5$ and $a/M = 0.7$. For smaller spins, since $\Delta t^{22}_{\rm peak}$ is small, the pQNM would be short lived and would not alter our results significantly.

As in the nonspinning case, phase and amplitude agreement are excellent until the ISCO. The phase differences remain small during the plunge, until merger, and grow up to ∼0.1 rad during the ringdown. The amplitude difference grows to larger values, ∼20–30% through merger and ringdown because of the limitations of our procedure to attach the QNMs in the EOB waveforms (see Ref. [28], Fig. 3 and associated discussion). The phase difference during the merger ringdown for the case $a/M = 0.7$ is larger because for larger and larger spins the resummed-factorized waveforms [15] perform less and less accurately

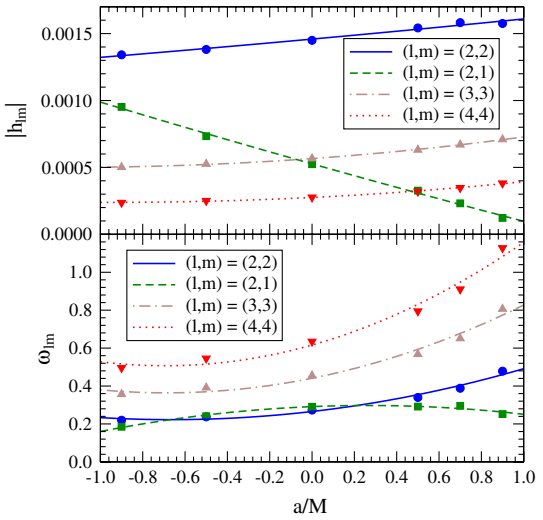

FIG. 13 (color online). Peak amplitude and corresponding frequency of Teukolsky modes as a function of spins. Top panel is the peak amplitude $|h^{\rm Teuk}_{\ell m,{\rm peak}}|$; bottom is the frequency $\omega^{\rm Teuk}_{\ell m,{\rm peak}}$ extracted when the amplitude reaches this peak. Data is for the (2, 2), (2, 1), (3, 3), and (4, 4) modes, for spins $a/M = -0.9$, -0.5, 0, 0.5, 0.7, and 0.9. Solid lines are quadratic fits to these; the fits are given in Eq. (56).

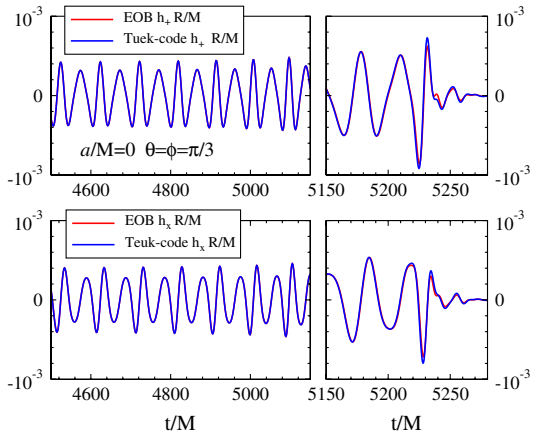

FIG. 14 (color online). Comparison between Teukolsky-calibrated EOB and Teukolsky h_+ and $h_\times$ polarizations for $a/M = 0$. The four dominant modes (2, 2), (2, 1), (3, 3), and (4, 4) are included.

around and beyond the ISCO. In the case $a/M = -0.9$, the disagreement between the EOB and Teukolsky (2, 2) becomes large and oscillatory during ringdown. This is a consequence of the fact that the oscillatory frequency behavior discussed in Sec. III E is particularly strong in this case, but we are not including the associated $(2, -2)$ QNMs in our EOB model.

Finally, although in this paper we do not attempt to calibrate higher-order modes for $a \neq 0$, it is useful for ongoing work on the comparable-mass case to extract relevant information, such as the time delay between the peaks of the (ℓ, m) modes and the input parameters entering the RHS of Eqs. (50)–(54). In Table VI, we show the time delays $\Delta t^{\ell m}_{\rm peak}$; in Fig. 13, we show $|h^{\rm Teuk}_{\ell m,{\rm peak}}|$ and $\omega^{\rm Teuk}_{\ell m,{\rm peak}}$ as functions of a/M. Quadratic fits to these functions are as follows:

$$
\begin{aligned}
|h^{\rm Teuk}_{22,{\rm peak}}| &= 0.001[1.46 + 0.144a/M + 0.00704(a/M)^2],\\
|h^{\rm Teuk}_{21,{\rm peak}}| &= 0.001[0.527 - 0.445a/M + 0.016(a/M)^2],\\
|h^{\rm Teuk}_{33,{\rm peak}}| &= 0.001[0.566 + 0.133a/M + 0.0486(a/M)^2],\\
|h^{\rm Teuk}_{44,{\rm peak}}| &= 0.001[0.276 + 0.0773a/M + 0.0405(a/M)^2],\\
\omega^{\rm Teuk}_{22,{\rm peak}} &= 0.266 + 0.129a/M + 0.0968(a/M)^2,\\
\omega^{\rm Teuk}_{21,{\rm peak}} &= 0.291 + 0.0454a/M - 0.0857(a/M)^2,\\
\omega^{\rm Teuk}_{33,{\rm peak}} &= 0.441 + 0.224a/M + 0.163(a/M)^2,\\
\omega^{\rm Teuk}_{44,{\rm peak}} &= 0.616 + 0.315a/M + 0.227(a/M)^2. \qquad (56)
\end{aligned}
$$

We postpone to future work the study of $d^2|h^{\rm Teuk}_{\ell m,{\rm peak}}|/dt^2$ and $\dot\omega^{\rm Teuk}_{\ell m,{\rm peak}}$ for higher-order modes.

V. CONCLUSIONS

The similarity of the transition from inspiral to merger to ringdown over all mass ratios studied in Refs. [8,11]

suggested the possibility of using the test-particle limit as a laboratory to investigate quickly and accurately the main features of the merger signal. The authors of Refs. [32,33] were the first to exploit this possibility. They proposed using the EOB inspiral-plunge trajectory to build the source for the time-domain Regge-Wheeler-Zerilli equations. They also improved the EOB modeling, notably the energy flux and the non-quasi-circular orbit effects, by requiring that the EOB and RWZ leading (2, 2) mode agreed during plunge, merger, and ringdown.

Here, we have employed the time-domain Teukolsky code developed in Refs. [39–41] and extended previous works [32,33,35,36] in several directions. In the Schwarzschild case, we first discussed how the EOB model developed in Ref. [28] for comparable-mass nonspinning black holes performs when $\nu = 10^{-3}$ for the leading (2, 2) mode, as well as for three subleading modes, (2, 1), (3, 3), and (4, 4). Confirming previous results [15,32–36,67,68], we found that the agreement between the Teukolsky and EOB modes is excellent during the long inspiral. During the merger, whereas the agreement of the (2, 2) and (3, 3) modes is still good, that of the (4, 4) and (2, 1) is not very satisfactory. We find that this is due to the irregular behavior of the numerical-relativity input values for the peak of the mode amplitude and the gravitational frequency at that peak. This motivates the need for more accurate numerical-relativity data for these higher-order modes, which will presumably be available in the future. By calibrating the EOB model using input values directly extracted from the Teukolsky modes (Tables II and III), we found very good agreement for the four largest modes. In Fig. 14, we compare h_+ and $h_\times$ constructed for these four modes, using

$$h_+(\theta, \phi, t) - i h_\times(\theta, \phi, t) = \sum_{\ell, m-2} Y_{\ell m}(\theta, \phi) h_{\ell m}(t). \quad (57)$$

The sum here is over $(\ell, m) = (2, \pm 2), (2, \pm 1), (3, \pm 3)$, and $(4, \pm 4)$. The agreement between EOB and Teukolsky polarizations is very good as expected. There are some minor differences during the ringdown, which are mainly due to the underestimated ringdown amplitudes of the (2, 2) and (3, 3) modes in the EOB model.

Moreover, for the first time, we employed the EOB inspiral-plunge trajectory to produce merger waveforms for quasicircular, equatorial inspiral in the Kerr spacetime. The energy flux in the EOB equations of motion uses the factorized resummed waveforms of Refs. [13,15]. We calibrated the leading EOB (2, 2) mode for spins $a/M = -0.9, -0.5, 0.5, 0.7$, and extracted information on the subleading modes. We also investigated the high spin case $a/M = 0.9$. We found that several modes which are subleading during the inspiral become relevant during plunge and merger. The major new feature of the EOB calibration (based on Teukolsky data) is that we relaxed the assumption used in previous papers [18–20,22–28] that the matching of the QNMs for the leading (2, 2) mode occurs at the peak of the orbital frequency. In fact, we found that the peak of the orbital frequency does not occur at the same time as the peak of the Teukolsky (2, 2) mode and that the time difference grows as the spin parameter increases. Our work represents a first step in exploring and taking advantage of test-particle limit results to build a better spin EOB model in the comparable-mass case [45].

In the future, we plan to extend this work in at least two directions. First, we want to calibrate the EOB model in the test-particle limit for higher spins and for higher-order modes and to connect it to the spin EOB model in the comparable-mass case [23,45]. To achieve this goal, we would need to introduce adjustable parameters in the functions $\rho_{\ell m}$ in Eq. (11) to improve the resummed-factorized energy flux and amplitude modes for large spin values.

In our future analyses, we will use a Teukolsky code which uses hyperboloidal slicing [36,53]. Although we were able to achieve similar accuracy by extrapolating our results from finite radius to future null infinity, hyperboloidal slicing is far faster and has proven to be very robust. Second, we would like to extend this model to inclined orbits. To tackle this case, we need to generalize the resummed-factorized waveforms to generic spin orientations. If we were only interested in extracting the input values, as in Tables IV and V, it might be sufficient to use the hybrid method suggested in Ref. [48]. In this case, we could use in the EOB equations of motion the energy flux computed with a frequency-domain Teukolsky code [61] but extend it to plunging trajectories.

Finally, besides improving the EOB model, the possibility of generating quickly and accurately merger waveforms in the test-particle limit will allow us to investigate several interesting phenomena, such as the distribution of kick velocities for spinning black-hole mergers [41], the energy and angular-momentum released when a test particle plunges into a Kerr black hole [74,75], and the *generic* ringdown frequencies suggested in Refs. [49,50].

ACKNOWLEDGMENTS

E. B., A. B., and Y. P. acknowledge support from NSF Grant No. PHY-0903631. A. B. also acknowledges support from NASA Grant No. NNX09AI81G. G. K. acknowledges research support from NSF Grant Nos. PHY-0902026, CNS-0959382, PHY-1016906, and PHY-1135664, and AFOSR DURIP Grant No. FA9550-10-1-0354. S. A. H. was supported by NSF Grant No. PHY-0449884 and NASA Grant No. NNX08AL42G; S. O. was also supported by NASA Grant NNX08AL42G. Most of the numerical simulations needed for this work were performed on Georgia Tech's Keeneland supercomputer under Project No. UT-NTNL0036.

[1] F. Pretorius, Phys. Rev. Lett. **95**, 121101 (2005).
[2] M. Campanelli, C. O. Lousto, P. Marronetti, and Y. Zlochower, Phys. Rev. Lett. **96**, 111101 (2006).
[3] J. G. Baker, J. R. van Meter, S. T. McWilliams, J. Centrella, and B. J. Kelly, Phys. Rev. Lett. **99**, 181101 (2007).
[4] S. Dain, C. O. Lousto, and Y. Zlochower, Phys. Rev. D **78**, 024039 (2008).
[5] G. Lovelace, M. A. Scheel, and B. Szilagyi, Phys. Rev. D **83**, 024010 (2011).
[6] C. O. Lousto and Y. Zlochower, Phys. Rev. Lett. **106**, 041101 (2011).
[7] A. Buonanno and T. Damour, Phys. Rev. D **59**, 084006 (1999).
[8] A. Buonanno and T. Damour, Phys. Rev. D **62**, 064015 (2000).
[9] T. Damour, P. Jaranowski, and G. Schäfer, Phys. Rev. D **62**, 084011 (2000).
[10] T. Damour, Phys. Rev. D **64**, 124013 (2001).
[11] A. Buonanno, Y. Chen, and T. Damour, Phys. Rev. D **74**, 104005 (2006).
[12] T. Damour, P. Jaranowski, and G. Schäfer, Phys. Rev. D **78**, 024009 (2008).
[13] T. Damour, B. R. Iyer, and A. Nagar, Phys. Rev. D **79**, 064004 (2009).
[14] E. Barausse and A. Buonanno, Phys. Rev. D **81**, 084024 (2010).
[15] Y. Pan, A. Buonanno, R. Fujita, E. Racine, and H. Tagoshi, Phys. Rev. D **83**, 064003 (2011).
[16] A. Nagar, Phys. Rev. D **84**, 084028 (2011).
[17] E. Barausse and A. Buonanno, Phys. Rev. D **84**, 104027 (2011).
[18] A. Buonanno, G. B. Cook, and F. Pretorius, Phys. Rev. D **75**, 124018 (2007).
[19] A. Buonanno, Y. Pan, J. G. Baker, J. Centrella, B. J. Kelly, S. T. McWilliams, and J. R. van Meter, Phys. Rev. D **76**, 104049 (2007).
[20] Y. Pan, A. Buonanno, J. G. Baker, J. Centrella, B. J. Kelly, S. T. McWilliams, F. Pretorius, and J. R. van Meter, Phys. Rev. D **77**, 024014 (2008).
[21] M. Boyle, A. Buonanno, L. E. Kidder, A. H. Mroué, Y. Pan, H. P. Pfeiffer, and M. A. Scheel, Phys. Rev. D **78**, 104020 (2008).
[22] A. Buonanno, Y. Pan, H. P. Pfeiffer, M. A. Scheel, L. T. Buchman, and L. E. Kidder, Phys. Rev. D **79**, 124028 (2009).
[23] Y. Pan, A. Buonanno, L. Buchman, T. Chu, L. Kidder, H. Pfeiffer, and M. Scheel, Phys. Rev. D **81**, 084041 (2010).
[24] T. Damour and A. Nagar, Phys. Rev. D **77**, 024043 (2008).
[25] T. Damour, A. Nagar, E. N. Dorband, D. Pollney, and L. Rezzolla, Phys. Rev. D **77**, 084017 (2008).
[26] T. Damour, A. Nagar, M. Hannam, S. Husa, and B. Brügmann, Phys. Rev. D **78**, 044039 (2008).
[27] T. Damour and A. Nagar, Phys. Rev. D **79**, 081503 (2009).
[28] Y. Pan, A. Buonanno, M. Boyle, L. T. Buchman, L. E. Kidder *et al.*, arXiv:1106.1021.
[29] N. Yunes, A. Buonanno, S. A. Hughes, M. Coleman Miller, and Y. Pan, Phys. Rev. Lett. **104**, 091102 (2010).
[30] P. Amaro-Seoane, B. Schutz, and N. Yunes, arXiv:1003.5553.
[31] N. Yunes *et al.*, Phys. Rev. D **83**, 044044 (2011).
[32] A. Nagar, T. Damour, and A. Tartaglia, Classical Quantum Gravity **24**, S109 (2007).
[33] T. Damour and A. Nagar, Phys. Rev. D **76**, 064028 (2007).
[34] S. Bernuzzi and A. Nagar, Phys. Rev. D **81**, 084056 (2010).
[35] S. Bernuzzi, A. Nagar, and A. Zenginoglu, Phys. Rev. D **83**, 064010 (2011).
[36] S. Bernuzzi, A. Nagar, and A. Zenginoglu, Phys. Rev. D **84**, 084026 (2011).
[37] T. Regge and J. A. Wheeler, Phys. Rev. **108**, 1063 (1957).
[38] F. J. Zerilli, J. Math. Phys. (N.Y.) **11**, 2203 (1970).
[39] P. Sundararajan, G. Khanna, and S. A. Hughes, Phys. Rev. D **76**, 104005 (2007).
[40] P. Sundararajan, G. Khanna, S. A. Hughes, and S. Drasco, Phys. Rev. D **78**, 024022 (2008).
[41] P. A. Sundararajan, G. Khanna, and S. A. Hughes, Phys. Rev. D **81**, 104009 (2010).
[42] S. Teukolsky, Astrophys. J. **185**, 635 (1973).
[43] J. McKennon and G. Khanna, Comput. Phys. Commun. **181**, 1605 (2010).
[44] E. Barausse, E. Racine, and A. Buonanno, Phys. Rev. D **80**, 104025 (2009).
[45] A. Taracchini *et al.* (unpublished).
[46] C. O. Lousto and Y. Zlochower, Phys. Rev. Lett. **106**, 041101 (2011).
[47] H. Nakano, Y. Zlochower, C. O. Lousto, and M. Campanelli, Phys. Rev. D **84**, 124006 (2011).
[48] W.-B. Han and Z. Cao, Phys. Rev. D **84**, 044014 (2011).
[49] Y. Mino and J. Brink, Phys. Rev. D **78**, 124015 (2008).
[50] A. Zimmerman and Y. Chen, Phys. Rev. D **84**, 084012 (2011).
[51] S. Hadar and B. Kol, Phys. Rev. D **84**, 044019 (2011).
[52] S. Hadar, B. Kol, E. Berti, and V. Cardoso, Phys. Rev. D **84**, 047501 (2011).
[53] A. Zenginoglu and G. Khanna, arXiv:1108.1816 [Phys. Rev. X (to be published)].
[54] Y. Pan, A. Buonanno, R. Fujita, E. Racine, and H. Tagoshi, Phys. Rev. D **83**, 064003 (2011).
[55] E. Berti, V. Cardoso, and C. M. Will, Phys. Rev. D **73**, 064030 (2006).
[56] W. Krivan, P. Laguna, P. Papadopoulos, and N. Andersson, Phys. Rev. D **56**, 3395 (1997).
[57] C. O. Lousto, H. Nakano, Y. Zlochower, and M. Campanelli, Phys. Rev. Lett. **104**, 211101 (2010).
[58] R. S. Alfio Quarteroni and F. Saleri, *Numerical Mathematics* (Springer-Verlag, New York, 2007), 2nd ed..
[59] M. Boyle, D. A. Brown, L. E. Kidder, A. H. Mroué, H. P. Pfeiffer, M. A. Scheel, G. B. Cook, and S. A. Teukolsky, Phys. Rev. D **76**, 124038 (2007).
[60] W. H. Press, S. A. Teukolsky, W. T. Wetterling, and B. P. Flannery, *Numerical Recipes in C* (Cambridge University Press, Cambridge, England, 1992), 2nd ed..
[61] S. A. Hughes, Phys. Rev. D **61**, 084004 (2000).
[62] S. Drasco and S. A. Hughes, Phys. Rev. D **73**, 024027 (2006).
[63] S. A. Hughes, Phys. Rev. D **64**, 064004 (2001).
[64] R. Fujita and H. Tagoshi, Prog. Theor. Phys. **113**, 1165 (2005).
[65] L. S. Finn and K. S. Thorne, Phys. Rev. D **62**, 124021 (2000).

[66] E. Barausse, V. Cardoso, and G. Khanna, Phys. Rev. D **84**, 104006 (2011).
[67] R. Fujita and B. R. Iyer, Phys. Rev. D **82**, 044051 (2010).
[68] R. Fujita, arXiv:1104.5615.
[69] S. Chandrasekhar and S. Detweiler, Proc. R. Soc. A **344**, 441 (1975).
[70] B. Mashhoon, Phys. Rev. D **31**, 290 (1985).
[71] S. Hod, Phys. Rev. D **80**, 064004 (2009).
[72] S. R. Dolan, Phys. Rev. D **82**, 104003 (2010).
[73] V. Cardoso, A. S. Miranda, E. Berti, H. Witek, and V. T. Zanchin, Phys. Rev. D **79**, 064016 (2009).
[74] A. Ori and K. S. Thorne, Phys. Rev. D **62**, 124022 (2000).
[75] M. Kesden, Phys. Rev. D **83**, 104011 (2011).